Estimating permeability in a limestone geothermal reservoir from NMR laboratory experiments

Maxime Catinat, Marc Fleury, Benjamin Brigaud, Miklos Antics, Pierre Ungemach

Estimating permeability in a limestone geothermal reservoir from NMR laboratory experiments

Maxime Catinat[a], Marc Fleury[b], Benjamin Brigaud[a], Miklos Antics[c], Pierre Ungemach[c]

[a]Université Paris-Saclay, CNRS, GEOPS, 91405 Orsay, France

[b]IFP Energies Nouvelles, 1-4 Avenue de Bois-Préau, 92852 Rueil-Malmaison, France

[c]GEOFLUID, 165 Rue de la belle étoile, 95700 Roissy CDG, France

Corresponding author: Maxime-catinat@hotmail.fr

Abstract

A wireline NMR (Nuclear Magnetic Resonance) logging tool has recently been deployed in the Dogger geothermal aquifer of the Paris Basin to provide a continuous permeability estimation throughout the reservoir. The complex pore structure of heterogeneous carbonate systems means that careful consideration must be given to standard permeability prediction. A laboratory study was performed on cores from a geothermal well at Bobigny, north of Paris. Petrographic and petrophysical analyses of thin sections, water permeability and laboratory NMR relaxation time T_2 were conducted on 72 samples. A classification was established using four main facies and the impact of microporosity and micritization on flow properties was investigated. The range of permeability is wide [0.05–1000 mD] and the evaluation addresses different relationships between permeability and a combination of porosity and T_2 distributions. Since the latter distributions can provide an estimation of the pore size distributions and in particular the fraction of microporosity within the total porosity, several possibilities arise for better constraining the permeability relationship. For one facies, permeability is nearly independent of porosity over a porosity range of [0.12–0.22], illustrating the well-known difficulty of predicting permeability in carbonate lithologies. The best permeability prediction is obtained when considering only macroporosity instead of total porosity in a classical power law.

Keywords: NMR, Geothermics, Limestones, Paris Basin, Petrography, Permeability.

1. Introduction

The Middle Jurassic (Dogger) carbonate reservoirs located at a depth of about 1.5 km were first identified in the 1980s as the most promising target for the development of geothermal energy in the Paris Basin (France) (Antics et al., 2005; Allo et al., 2021; Giot and Rojas, 1981; Housse and Maget, 1976; Lopez et al., 2010; Rojas et al., 1989). Fifty-four district heating production units with their associated wells and distribution grids exploit the heat capacity of a deep reservoir at 55–80 °C formed by the Bathonian limestones (Lopez et al., 2010; Rojas et al., 1989; Thomas et al., 2023). In order to improve our understanding of the heterogeneities in this reservoir, an NMR logging tool (Combinable Magnetic Resonance - CMR©) was deployed in two recent geothermal operations at Cachan in 2017 and Bobigny-Drancy in 2020 (Ungemach et al., 2019; Wielemaker et al., 2020). Whereas NMR logging data are routinely acquired in the petroleum industry (Appel et al., 2003), this is not a common practice when drilling geothermal wells, and especially in the central part of the Paris Basin where this is the first time such data have been acquired for the Bathonian geothermal reservoir.

When used in open hole logging, the NMR logging tool provides crucial data such as continuous porosity (ϕ), permeability (k), pore-size distribution and fluid saturation values (Kenyon, 1997; Nurmi and Standen, 1997; Westphal et al., 2005). Permeability is a key parameter when assessing geothermal performance but it is notoriously difficult to determine it from well logging data in carbonate systems (Lucia, 2007; Minh et al., 1997). Fundamentally, the NMR relaxation time T_2 distribution measured by the logging instrument is a proxy for the pore-size distribution and therefore it provides key information for evaluating permeability. It is still an indirect measurement but it is much more relevant than porosity alone. The porosity-permeability relationship in carbonate systems is far more complex than in sandstones and it varies with both facies and diagenetic effects (Ehrenberg and Nadeau, 2005). Hence the standard NMR-porosity-T_2 relationship should be carefully applied and/or calibrated with the testing of core samples. Once completed and an adequate understanding of the depositional environment and

the geological context have been gained, it can be applied safely to other wells for which NMR logs are available (Duan et al., 2018; Moss, 2000; Müller-Huber et al., 2016, 2018; Soete et al., 2021; Tian et al., 2018; Vincent et al., 2011).

A previous study in which cores were recovered from a Paris Basin geothermal reservoir (Bathonian) dates from 1981 at the Aulnay-sous-Bois doublet (Giot and Rojas, 1981). Petrography and porosity-permeability features were described providing a sound assessment of the productive (profitable) sections (Giot and Rojas, 1981; Robelin and Giot, 1987; Rojas et al., 1987). As a consequence, coring is seldom undertaken in the Bathonian geothermal aquifer and no NMR laboratory analyses on cores from the Middle Jurassic geothermal reservoir of the Paris Basin had been carried out prior to the present survey. The only NMR investigation of the Middle Jurassic limestones was performed on limestone in the eastern part of the Basin, about 250 km east of Paris (Brigaud et al., 2014). It then became necessary and urgent to calibrate the T_2 distributions in cores from the geothermal aquifer. During the recent geothermal operation at Bobigny, a suburb north of Paris, a 36 m core-section was drilled in the geothermal reservoir (*Oolithe blanche* Formation) in well GBD4.

The main objectives of this paper are (1) to supply a reference classification linking laboratory NMR T_2 distributions to geological observations derived from core samples for the geothermal carbonate reservoir, and (2) to derive an optimized relationship between NMR data, porosity and permeability providing reliable inputs for geothermal reservoir geomodelling. Once the geothermal reservoir models are constructed, they can be used for predictive heat and mass transfer simulations for future sustainable geothermal exploitation.

2. Geological and geothermal setting

The Paris Basin is a large intracratonic basin that is both stable and little modified by tectonic processes, covering a vast area of northern France of about 110 000 km^2. It is bounded by crystalline massifs (the Vosges, Armorican massif and Massif central) and filled with about 3000 m of sediments from Triassic to Quaternary Formations in the depocenter (Guillocheau et al., 2000; Mégnien and Mégnien, 1980). In the central part of the basin, 200 m-thick Middle Jurassic limestones are located at a depth of ca. 1500 m (Fig. 1A). The Bathonian deposits form the preferentially targeted aquifers for geothermal exploitation in the Middle Jurassic limestones (Lopez et al., 2010; Rojas et al., 1987; Thomas et al., 2023). During Bathonian times, the Paris Basin was an epicontinental sea located at subtropical latitudes. These climatic conditions promoted the development of the western Armorican and Burgundian shallow marine carbonate platforms (Brigaud et al., 2014; Contini et al., 1980; Vincent et al., 2021). From the most internal lagoonal facies to the most external lower offshore facies, the Bathonian deposits can be divided into three separate geological formations that can be situated along a theoretical carbonate ramp profile: (1) *Calcaires de Comblanchien*, (2) *Oolithe Blanche* and (3) *Calcaires marneux à Pholadomyes* (Thomas et al., 2023). The *Calcaires de Comblanchien* consist of peloidal to oncoidal facies mostly deposited in lagoonal areas, whereas the *Oolithe Blanche* Formation consists of ooid or bioclastic-dominated grainstones deposited in shoreface or shoal environments. The *Calcaires marneux à Pholadomyes* consist of marls and mud-dominated limestones facies mostly deposited in upper offshore settings. The *Oolithe Blanche* Formation in the basin centre is known to have the best reservoir properties as revealed by geothermal projects in the past few years (Hamm, 2015). In the Paris region, the vast majority of geothermal operations using doublet technologies reach the Middle Jurassic limestones which have high geothermal potential with fluid temperatures of up to 80 °C (Bonté et al., 2010, 2013; Lopez et al., 2010) in the deepest areas (Fig. 1A). They mainly supply district heating grids in densely urbanized and populated areas (Lund and Toth, 2021). Two recent geothermal operations (engineered and field supervised by GPC IP/GEOFLUID) have been completed at Bobigny, a Parisian suburb in the Seine-Saint-Denis (93) *département*, with the drilling of four new deviated wells in 2020 (GBD1,3: production; GBD2,4: injection) (Fig. 1B). The GBD1, GBD2 and GBD4 wells were drilled from ca. 1690 m to 1750 m depth in the Middle Jurassic limestone and the GBD3 well as far down as the Triassic (top of the Rhaetian) at ca. 2120 m depth (Fig. 1B). A 36 m-long core was extracted from the *Oolithe Blanche* Formation in well GBD4.

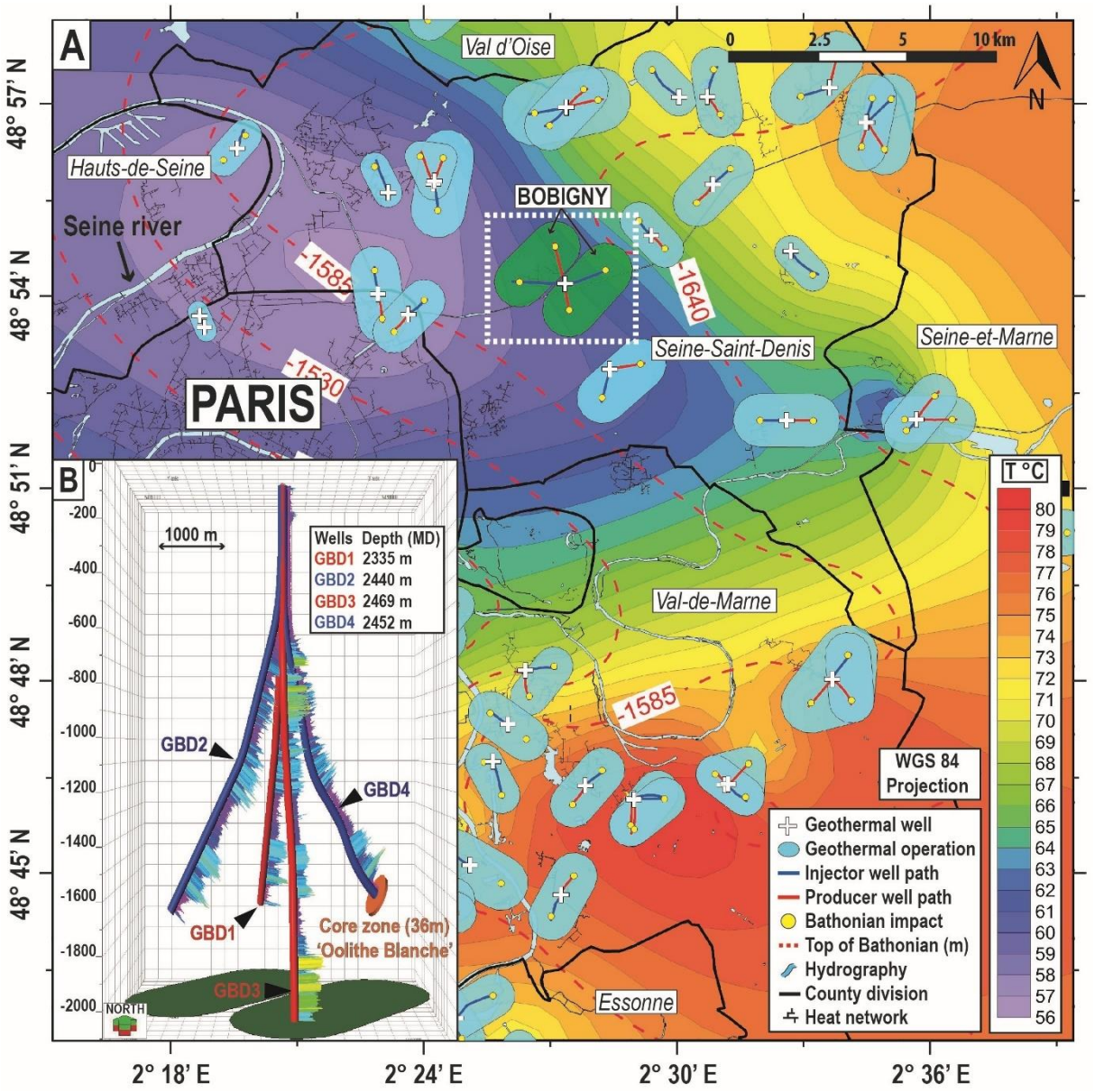

Fig. 1: A: Location map of geothermal wells producing the Bathonian geothermal waters. The temperature map of the geothermal water has been obtained by kriging from the Greater Paris area, illustrating the high density of geothermal wells supplying extensive district heating grids. Depending on locations, temperatures range from 56 to 80 °C. Note the colour code defining injection wells in blue and production wells in red. B: 3D architecture view and trajectories of Bobigny doublets. The interval of the core zone from the Oolithe Blanche Formation in GBD4 is in orange. The logs along the wells are gamma-ray logs. World Geodetic System 84 coordinates of well heads: GBD1 (X: 2.4549089; Y: 48.9039652), GBD2 (X: 2.4547782; Y: 48.9039412), GBD3 (X: 2.4550396; Y: 48.9039892), GBD4 (X: 2.4551703; Y: 48.9040123).

3. Materials and methods

3.1. Cores and petrographic investigations

A 36 m-long cored section was retrieved from deviated geothermal well GBD4 (Fig. 1B). This section has been described in detail in terms of grain composition and textures using 72 samples collected every 0.5 m and numbered from 1 to 72. From each full-size core, a cylindrical plug was extracted along the z axis (i.e. z being the longitudinal direction of the core, 25° inclination), without considering any x or y directions thus involving only 25° inclined permeability measurements (i.e. x and y being the two perpendicular directions which are transversal to the core). The diameter and length chosen for each core-plug were uniform and set to a standard size of 4 cm for the diameter and about 6 cm for the length. A total of 72 plugs were used for petrophysical measurements.

Petrographic investigations were made using light microscopy on thin sections to provide a better understanding of the geological components of facies such as textures, allochems (bioclastic, non-bioclastic), grain size, pore-type distributions and diagenetic features in carbonate rocks (Vincent et al., 2011; Wadood et al., 2021). For this study, standard thin sections (30 µm thick) impregnated with blue-stained epoxy resin were used to reveal the micropore and macropore networks. Several thin section pictures were taken and assembled using Image Composite Editor® software to get an overview of each sample thus facilitating observations. The JMicroVision© software was used to measure an arithmetic mean grain size for each thin section. Mercury injection capillary pressure (MICP) measurements have also been performed on four specific samples (n°2, 30, 43 and 45) to provide pore throat diameter (in µm) distributions. The texture of the samples was described using the Dunham (1962) and Embry and Klovan (1971) classifications and the pore spaces based on Choquette and Pray (1970) and Lønøy (2006) nomenclatures discriminating intraparticle porosity (pores within components), interparticle porosity (pores between components) and mouldic porosity. A total of 41 thin sections were observed (i.e. approximately 1 thin section per metre).

3.2. NMR principles and laboratory measurements

3.2.1. NMR principles and applications

Nuclear Magnetic Resonance (NMR) refers to the measurement of magnetization decays generated by hydrogen nuclei filling the pore space. These decays can be measured by a tool comprising a static magnetic field generated by permanent magnets and an oscillating magnetic field generated by an antenna at the Larmor frequency (Dunn et al., 2002). The measured magnetization decays can be described by exponential curves with characteristic times T_2 called transverse relaxation times. They are measured by both the logging tool and laboratory instruments in similar conditions (brine-water of about ca. 20 g/l NaCl and resonance frequency of ca. 2 MHz) so they can be compared and interpreted directly. The T_2 relaxation times obtained from NMR measurements at low magnetic field strength have long been recognized as a permeability indicator in combination with porosity (for a review, see Babadagli and Al-Salmi, 2004). Acquisition of such information by logging tools in open hole conditions has significantly improved permeability prediction from well-logging data. The main reason is that the relaxation time T_2 is a proxy of the pore size according to (Godefroy et al., 2001):

$$\frac{1}{T_2} = \rho_2 \frac{S}{V} + \frac{1}{T_{2B}} \quad [1]$$

where T_2 is the relaxation time measured in a single pore of volume V and surface area S, T_{2B} is the relaxation time of the bulk liquid saturating the pore ($T_{2B} \cong 3000$ ms for water at 30 °C), and ρ_2 is the surface relaxivity, a property of solid-liquid NMR interactions. The ratio V/S has a length dimension and characterizes the pore body which is different from the pore throat governing permeability. Where there are multiple pore sizes, magnetization decay curves from each pore can be summed and then plotted as a function of time, and the distribution of relaxation time T_2, can be obtained from this curve by a mathematical inversion process reflecting the distribution of pore sizes in the saturated porous media. The longer the magnetization decay times, the larger the pores. Conversely, the shorter the magnetic decay times, the smaller the pores. As will be shown later, the range of measurable relaxation times is adequate for evaluating both micro- and macroporosity in carbonate systems. Then, for evaluating permeability k, the following type of relationship can be used:

$$k = C\ \phi^a\ T_R^b \quad [2]$$

where ϕ stands for porosity, T_R is a relaxation time calculated from the measured distribution and expressing one representative pore size governing permeability; there are a large number of other formulas (Babadagli and Al-Salmi, 2004) and equation [2] is suitable for a formation saturated with a single liquid (brine in the present case) whereas many others deal with a formation saturated with oil and water for hydrocarbon production applications. Equation [2] has proved quite successful in sandstones and for these formations, the relaxation time T_R is chosen as the log mean value T_{2lm} of the distribution (Dunn et al., 2002). The significance of this choice is related to the existence of clays and if the amount of lining clays increases in the intergranular pore space, T_{2lm} will decrease and yield lower values. As a result lower permeabilities are calculated even though porosity may not vary much. For carbonates, there could be a similar rationale dealing with microporosity and by default, in the absence of cores for calibrating C, a and b in equation [2], their values are set to C = 4, a = 2, b = 4 and $T_R = T_{2lm}$ (with units k in mD, T_{2lm} in ms and porosity as a volume fraction). This relation is called the SDR (Schlumberger-Doll Research) default relationship (Kenyon et al., 1988), with the coefficient C adapted to carbonates as opposed to sandstones to take into account essentially the lower surface relaxivity of carbonates. The SDR equation has a theoretical basis derived from grain packing theory (Banavar and

Schwartz, 1987; Chauveteau et al., 1996) and as such it should be regarded as a guide only; the exponents a and b however are not universal, especially in the context of carbonates. For example, for a dataset of carbonates from the Middle East, T_R was chosen as the mode of the distribution T_{2mode} and a = 0.60, b = 2.44 (Fleury et al., 2001). For more detailed descriptions on the NMR physics, readers may refer to the publication by Vincent et al. (2011).

3.2.2. Laboratory measurements and statistical analysis

After saturating each plug with brine (20 g/l NaCl), water permeabilities (k_w) and formation factors were measured on 72 samples in a flooding cell equipped with electrodes at both ends to measure resistivity (formation factor results will not be discussed here). T_2 relaxation time distributions were measured on the same 72 samples using a Magritek instrument (Wellington, New Zealand) with a proton resonance frequency of 2 MHz, similar to that of the NMR logging instrument. Each sample thus presents its own T_2 relaxation time signature. By way of illustration, a distribution is shown in Fig. 2 in which the mode (T_{2mode}), the logarithmic mean time (T_{2lm}) and the cut-off value separating micro- and macroporosity (T_{2cm}) set in this study at the value of 120 ms are indicated. This cut-off is between the default value used in log interpretation (Dunn et al., 2002) and the value proposed by Vincent et al., (2011) (i.e. 200 ms) based on various outcrop carbonates. It corresponds also to the minimum for most distributions as shown later in Fig. 5. For the example shown in Fig. 2, the cut-off could be chosen at the minimum of the distribution near 80 ms and for other samples, the minimum is located at a much larger value (e.g. 150 ms). For section 4.2. particularly, it is also important to mention that 15 permeability values of 0.02 mD were omitted; for such low permeability, the equipment used for the measurements was not adequate and would have required a specific system with appropriate pressure sensors and pumps; hence only upper values are indicated. Extending porosity-permeability relationships in the low and very low permeability range is not of great interest in the present context and keeping these data when calculating the various correlations would generate a bias. These samples have also a small macropore volume, on average 14% of total porosity, and the macropore network may not be continuous and therefore not contribute to the flow. The total porosity of a sample is obtained from the ratio of the pore volume measured by NMR and the volume of the cylindrical plug. In Fig. 2, it corresponds to the sum of all amplitudes in the T_2 distribution. Macroporosity is obtained from the sum of amplitudes for $T_2 > T_{2cm}$.

In order to identify groups with similar NMR distributions, the statistical k-means algorithm classifying a dataset on the basis of a pre-defined number of ‘k’ clusters, was used (Macqueen, 1967; Sarker, 2021). Clustering is done using this algorithm in Matlab©, independently of facies attribution (i.e. each T_2 distribution was grouped into k classes). A classification quality control has been done using the “Silhouette” function on Matlab© providing information for a good or bad NMR T_2 distribution assignment to a cluster.

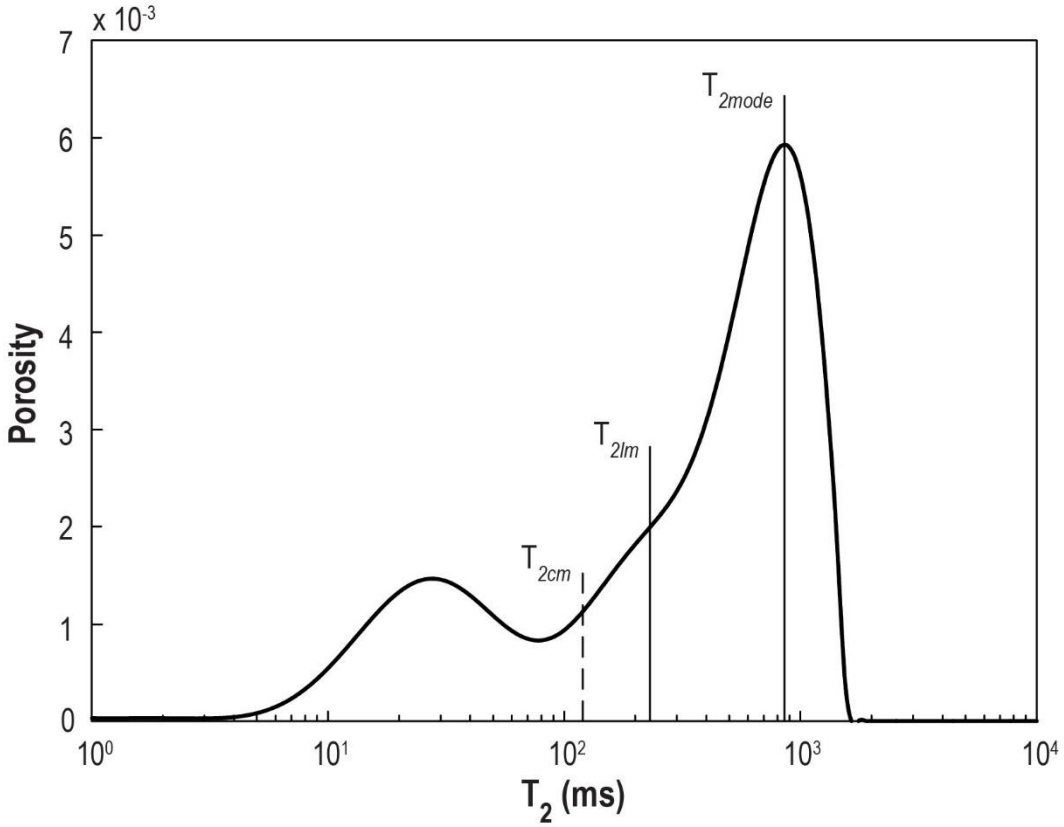

Fig. 2: Example of a distribution measured in the laboratory for a sample of the Dogger Formation (depth 2383.7 m); the log mean value T_{2lm} and the mode T_{2mode} of this distribution are indicated by vertical lines. The cut-off T_{2cm} for separating micro- and macroporosity is also shown.

4. Results and discussions

4.1. Geological aspects

4.1.1. Sedimentary facies

Detailed sedimentological observations from core descriptions allowed to define four facies covering a wide range of sedimentary textures and granulometries. These range from coarse-grained limestones (i.e. dominantly grainstones), sometimes presenting grains larger than 2 mm (i.e. rudstones), to fine and mud-supported limestones with variable grain sizes (i.e. packstone to floatstone textures). These textures are indicative of two depositional processes that can be found on a downdip carbonate ramp profile. All the facies were described in terms of allochems, texture, sorting, grain size, pore-type, pore throat diameter (in µm) and diagenetic cements. All observations and descriptions are summarized in Table 1. The detailed mean grain size and MICP results are summarized in Supplementary Tables A and B, respectively.

Firstly, two limestone facies were identified (1) microporous oncoidal and peloidal packstones to rudstones (F1a, Fig. 3A-C) and (2) slightly porous oncoidal packstones to floatstones (F1b, Fig. 3B-D). These facies consist mostly of bioclastic limestones, locally intercalated with thin marl interbeds (decimetre thick). The dominant fauna is composed of bivalves, echinoderms, brachiopods, gastropods, bryozoans, coral fragments and foraminifers, indicating normal oxygenation and salinity of marine waters. These facies were related to an upper offshore zone located on the mid-ramp deposited between the lower storm wave base and the upper fair-weather wave base boundaries. They were thus grouped into an unique facies association FA1 (mud-dominated facies). In terms of pore-type, facies F1a presents abundant microporosity invading mainly the micritic matrix and oncoid/ooid cortex (Fig. 3C), whereas facies F1b is characterized by rare mouldic/intrafossil pores (e.g. sample n°43), some microporosity in the micritic matrix, but no macropores (Fig. 3D). Scarce dolomite dissolution, heterogeneously distributed, is also observed in facies F1a (samples n°18, n°20 and n°50). For facies F1a (sample n°45), the pore throat diameter distribution is faintly bimodal with a dominant mode at about 0.1 µm (see Supplementary Table B). Pore throat diameter distributions of samples n°30 and 43 are

similar, slightly bimodal, with a dominant mode at low values, between 0.1 µm and 0.2 µm (see Supplementary Table B).

The second facies association (FA2) is characterized by oolithic grainstones deposited in a high-energy shoreface and/or shoal environment in an inner ramp position above the fair-weather wave base. Based on the progressive reduction of pore spaces by diagenetic cement development between the grains, two facies were differentiated, namely (1) low to moderately cemented ooid grainstone (F2a) and (2) highly porous ooid grainstone (F2b) representing the facies associated with the best reservoir quality which is very typical of the *Oolithe Blanche* Formation. Both F2a and F2b contain high proportions of concentric ooids (Fig. 3G-H). In facies F2a, rhombohedral pore spaces of 50 µm–1.5 mm in size are observed in 10 samples (Fig. 3G). This geometric rhombohedral shape of pore is typical of dissolution of dolomite rhombs (Purser, 1985). This dissolution process may be deduced by examination of void shapes and boundaries (Purser, 1985). The original rhombic pseudomorphs may be only preserved locally, either as "flat surfaces" printing the crystal faces or as "points" printing the crystal terminations (Fig. 4A-B-C). These rhombohedral pore spaces may be labelled as mouldic (Fig. 3G). Especially within a restricted interval of nearly 2 meters, 5 samples (n°12, 13, 14, 15 and 17) present frequent mouldic rhombohedral pores associated to dolomite dissolution. This dolomite dissolution is heterogeneously distributed in thin-section, and significantly enhances the porous media (i.e. no specific distribution is evidenced based on petrographic observations). Such dolomite dissolution features are relatively common in Middle Jurassic limestones of the Paris Basin, producing a secondary pore system (Purser, 1985). Dolomite dissolutions in Bathonian limestones have been reported around Coulommes, 50 km east of Paris (oilfield), Melun, 50 km south-east of Paris (geothermal reservoir) and Aulnay-sous-Bois, 10 km north-east of Paris (geothermal reservoir), but also in outcrops along the southeastern part of the Paris basin (Giot and Rojas, 1981; Purser, 1985; Thomas et al., 2023). In facies F2a, blocky calcite and syntaxial overgrowth cements around echinoderm fragments are frequent and reduce the pore spaces (Fig. 4D). In facies F2b, blocky calcite is rarer and a few syntaxial cements are also developed around echinoderm fragments (Fig. 3H). A few dolomite dissolution rhombs, sparsely distributed, are also observed in facies F2b (only within sample n°4) and the dominant mode of pore throat diameter (measured in sample n°2) is nearly equal to 50 µm, corresponding to the connections between macropores (see Supplementary Table B). The proportion of intergranular porosity in facies F2a is high and very high in facies F2b.

Depositional environments and corresponding facies association	Facies	Non-bioclastic components	Bioclastic components	Energy and depositional environments (Burchette and Wright, 1992)	Sorting and grain size (Mean– Std)	Pore-type and pore throat diameter (Mode in µm)	Diagenesis
Upper Offshore, Palaeodepth 30–50 m, Mud-dominated facies (Facies association FA1)	F1a – Microporous oncoidal and peloidal packstone to rudstone	Concentric Ooids (C), Peloids (F), Oncoids (C), Superficial Ooids (C), Composite Ooids (R), Lumps (R), Intraclasts (R), Hydrocarbon trace (?)	Bivalves (F), Echinoderms (C), Foraminifers (C), Gastropods (R), Spicules (R), Bryozoans (R), Brachiopods (R), Trichites (R)	Low to moderate energy, Upper Offshore	Poorly sorted to well sorted, 600 µm–180 µm	Abundant interparticle microporosity (micritic matrix) and intraparticle microporosity (ooid cortex), rare intergranular porosity; pore throat diameter: 0.1 µm	Low micritization of grains, local blocky calcite and syntaxial cement (echinoderms), rare dolomite and bioclast dissolution, stylolitization
	F1b – Slightly porous oncoidal packstone to floatstone	Oncoids (A), Peloids (F), Ooids (R), Composite Ooids (R), Intraclasts (R)	Bivalves (F), Crinoids (C), Gastropods (C), Bryozoans (C), Brachiopods (C), Corals (C), Foraminifers (R), Microbial encrustation (R), Leiolithes (R), Burrows (R)	Low to moderate energy, Upper Offshore	Very poorly sorted, 730 µm–250 µm	Mouldic porosity (high in coral fragments) and some microporosity in the micritic matrix; pore throat diameter: between 0.1-0.2 µm	Medium micritization, local blocky calcite, syntaxial cement (echinoderms), intragranular microsparitic cement
Shoal Environment/ Shoreface, Ooid-dominated facies, Palaeodepth <30 m (Facies association FA2)	F2a – Low to moderately cemented ooid grainstone with bioclasts	Concentric Ooids (A), Peloids (C), Oncoids (R), Composite Ooids (R), Intraclasts (R)	Echinoderms (F), Bivalves (C), Brachiopods (C), Foraminifers (R)	Medium to high energy, wave dominated, Shoal	Moderately sorted to well sorted, 410 µm–120 µm	Interparticle macroporosity, local intraparticle microporosity, local mouldic porosity (rhomboedral pore space)	Local to well-developed blocky calcite, syntaxial cement (echinoderm), important dolomite dissolution
	F2b – Highly porous ooid grainstone	Concentric ooids (A), Peloids (R)	Echinoderm fragments (C)	High energy, wave dominated, Shoreface/ Shoal near sea surface	Very well sorted, 350 µm–70 µm	Abundant interparticle macroporosity; pore throat diameter: 50 µm	Rare cement, rare ooid micritization, very rare ooid nucleus dissolution and rare dolomite dissolution

Table 1: Facies classification according to core descriptions. A: abundant; C: common; F: frequent; R: rare. Std: standard deviation.

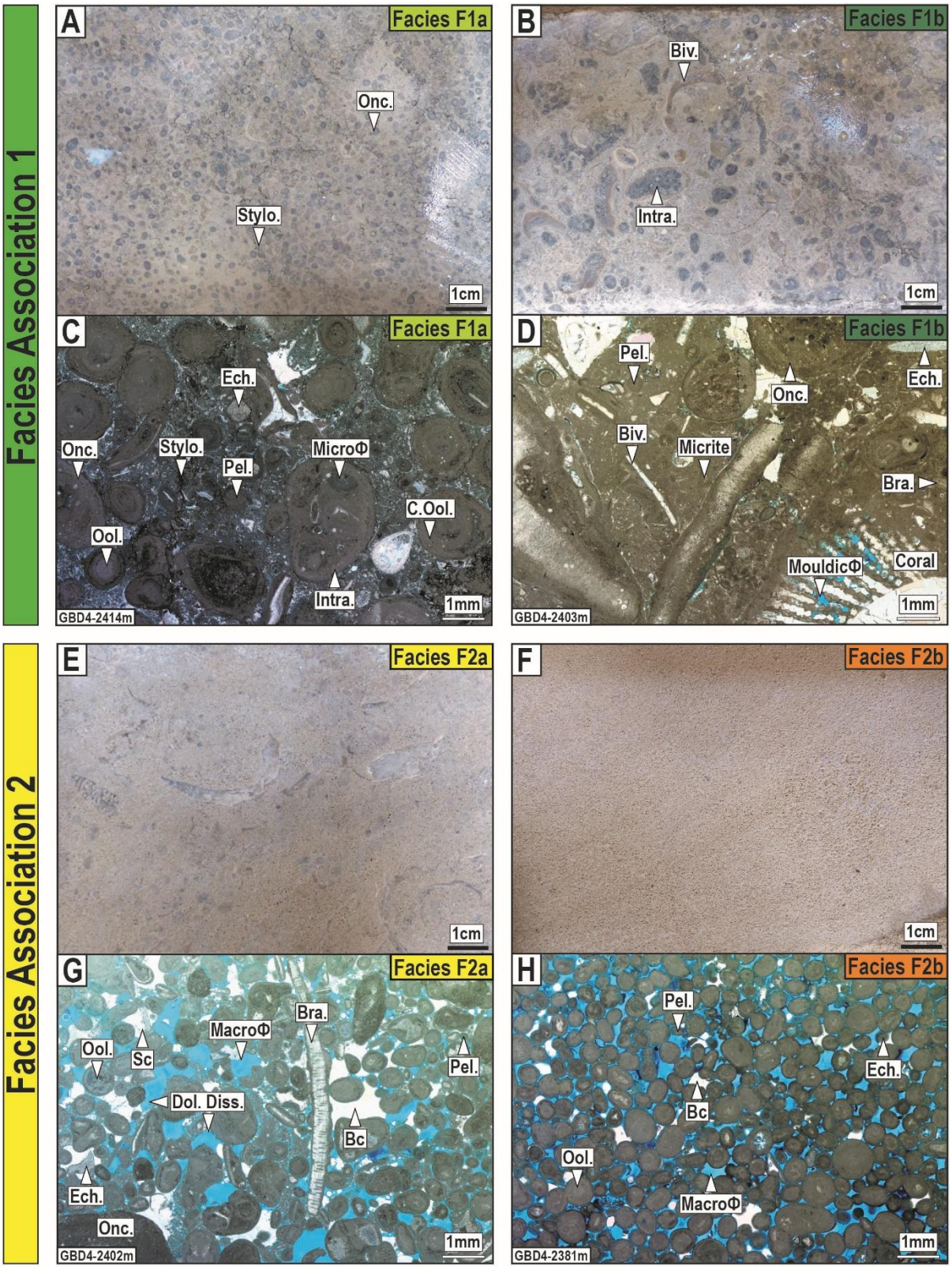

Fig. 3: Petrographic characteristics of core samples from Bobigny 4 well (GBD4). Depths of each thin section are indicated in the bottom left corner and the related facies in the top right corner. A: Core picture showing a microporous oncoidal rudstone with most grains larger than 2 mm linked to the mud-dominated facies association FA1. B: Core picture showing a slightly porous oncoidal and bioclastic floatstone linked to the mud-dominated facies association FA1. C: Microphotograph from A, illustrating heterogeneous peloidal (Pel.) and oncoidal (Onc.) packstone to rudstone. Note the presence of echinoderm fragments (Ech.) and millimetric muddy intraclasts (Intra.). The presence of stylolites (Stylo.)

filled with organic matter in the micrite texture and in contact with grains are markers of compaction accommodation during burial. This sample is mostly characterized by microporosity (Micro ϕ) affecting the micritic matrix. Note also the intraparticle micropore network revealed by the blue-stained resin impregnation within oncoids and composite-ooid cortexes (C.Ool., Ool.). D: Microphotograph from B, illustrating an oncoidal floatstone. The allochems are very largely unsorted, from micrometric to centimetric, and they are floating in a muddy matrix. Within this sample, six types of allochems are present: pellets (Pel.), oncoids (Onc.), echinoderms (Ech.), brachiopods (Bra.), bivalves (Biv.) and corals. Contrary to facies F1a, non-homogeneous intra-interparticle microporosity is observed. Rare mouldic porosity (Mouldic ϕ) such as in coral debris is preserved, but most of the potentially mouldic pores are completely filled with blocky calcite or microsparitic cement. E: Core picture showing an ooidal to peloidal grainstone with moderately sorted bioclasts presenting more locally cemented patches (facies association FA2). F: Core picture showing a very well sorted and highly porous ooid-rich grainstone (facies association FA2). G: Microphotograph from E of an oolithic grainstone with well-developed syntaxial overgrowth cement (Sc) around non-micritized echinoderm (Ech.) fragments and patchy cemented areas (Bc: Blocky calcite). Note the rhombohedric shape of certain pores truncating the particles, probably resulting from dolomite dissolution processes (Dol. Diss.). Note also the interpenetrated structure of ooids and the micritization process. H: Microphotograph from F, illustrating an ooid-rich grainstone with well-developed macroporosity (Macro ϕ). In constrast with facies F2a, blocky calcite and syntaxial cements are less developed, enhancing the pore volume and there are more ooids than pellets and bioclasts. Note also the rare ooid nucleus dissolution.

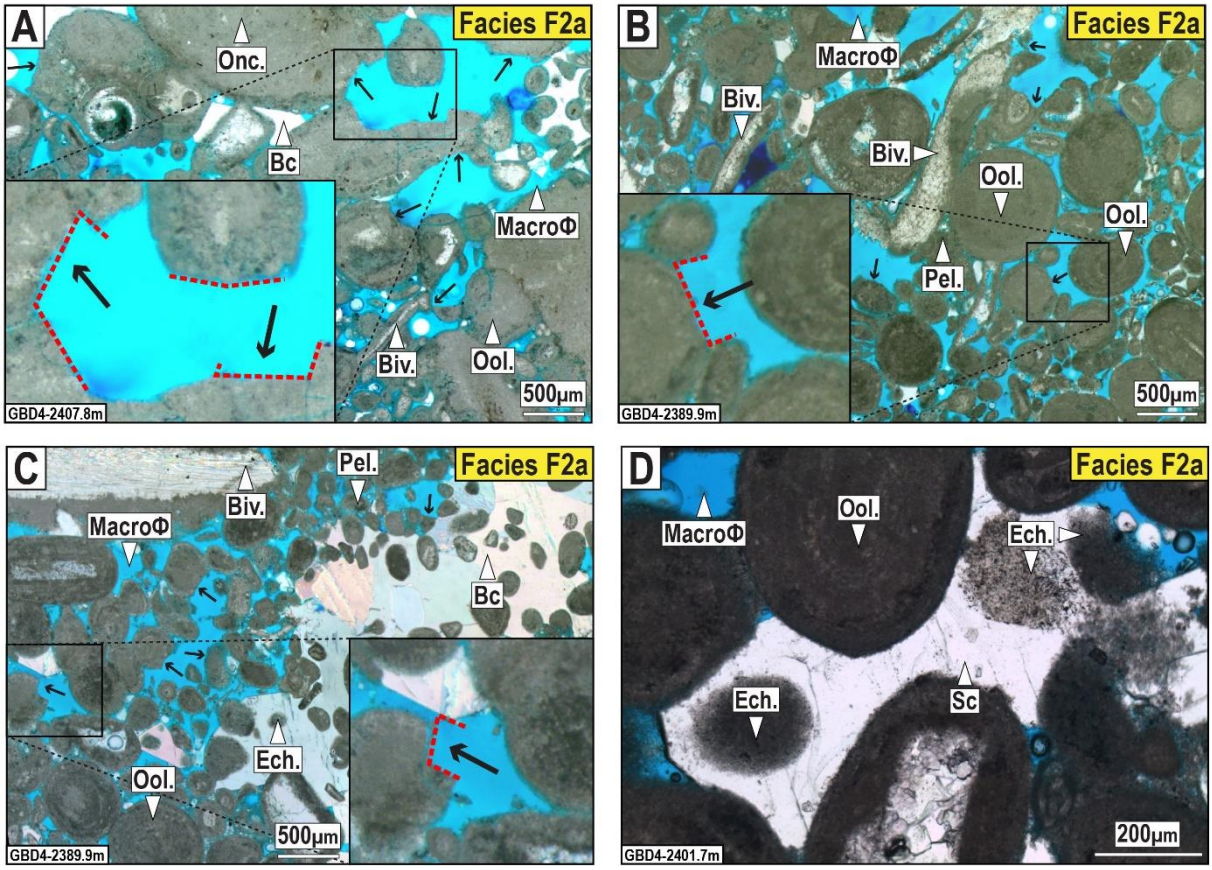

Fig. 4: Typical petrographic features of facies F2a. A, B and C: Microphotographs illustrating rhombohedral pore spaces limited by “flat surfaces” (printing the dissolved crystal faces) or by “points” (printing the dissolved crystal terminations) (see arrows and zooms). D: Microphotograph illustrating syntaxial overgrowth cements (Sc) around echinoderm fragments (Ech.) reducing the pore spaces.

4.1.2. Linkage between NMR signature, porosity, permeability and sedimentary facies

Experimental measurements derived from core plugs are displayed in Fig. 5 as a function of depth such as for logging data. Numerical values are listed in Supplementary Tables A, C and D. The vertical facies succession displayed includes F1a, F1b, F2a and F2b. Respectively, the ranges of values for each variable are: mean grain size from 0.2 mm to 1.2 mm, porosity from 4.3% to nearly 22%, permeability

from 0.005 mD to 900 mD, T_{2mode} and T_{2lm} values respectively from 10 ms to 1665 ms and from 7 ms to nearly 400 ms.

Normally, permeability is high when porosity is high. Two high porosity-permeability intervals (> 10% and k_w > 100 mD), named respectively “Reservoir 1” (2381–2390 m) and “Reservoir 2” (2407–2413 m), are identified. These levels are characterized by facies F2a and F2b, indicating that the highest porosity and permeability values are found in the ooid-dominated facies (FA2). In addition, a thinner intermediate level, located at 2402 m and also related to facies association FA2, shows significant permeability exceeding 10 mD. In contrast, levels defined by low porosities (4.3% < ϕ < 10%) and permeabilities (0.005 mD < k_w < 1 mD) are characterized by facies F1a and F1b (mud-dominated facies). These observations are in agreement with NMR T_2 pore-size distributions, i.e. the reservoir levels are visually well developed by signals with dominant T_{2mode} (i.e. amplitude peaks) with relaxation times exceeding 120 ms (i.e. T_{2cm}). Conversely, the signals with a T_{2mode} of less than 120 ms, detecting microporosity in samples, are characteristic for the lowest porosity and permeability intervals. These observations are clearly highlighted by juxtaposing T_{2mode} and T_{2lm} data, wherever there is a positive gap, by subtracting T_{2mode} from T_{2lm} for Reservoirs 1 and 2 (T_{2mode} > T_{2lm} connoting a dominant macropore volume), and a negative one for intermediate intervals (T_{2mode} < T_{2lm} connoting a dominant micropore volume). The Reservoirs 1 and 2 are characterized by samples with the smallest grain sizes (with a mean grain size of 0.37 mm) whereas intermediate layers exhibit higher values (with a mean of 0.64 mm). Facies F2b in Reservoir 1 displays the largest pore throat diameter with 50 µm corresponding to the connections between macropores. The highest mean grain size value (of nearly 1.2 mm) is observed in sample n°43 located at 2403 m, and the lowest in sample n°15 (of nearly 0.24 mm) at 2389 m (Fig. 5).

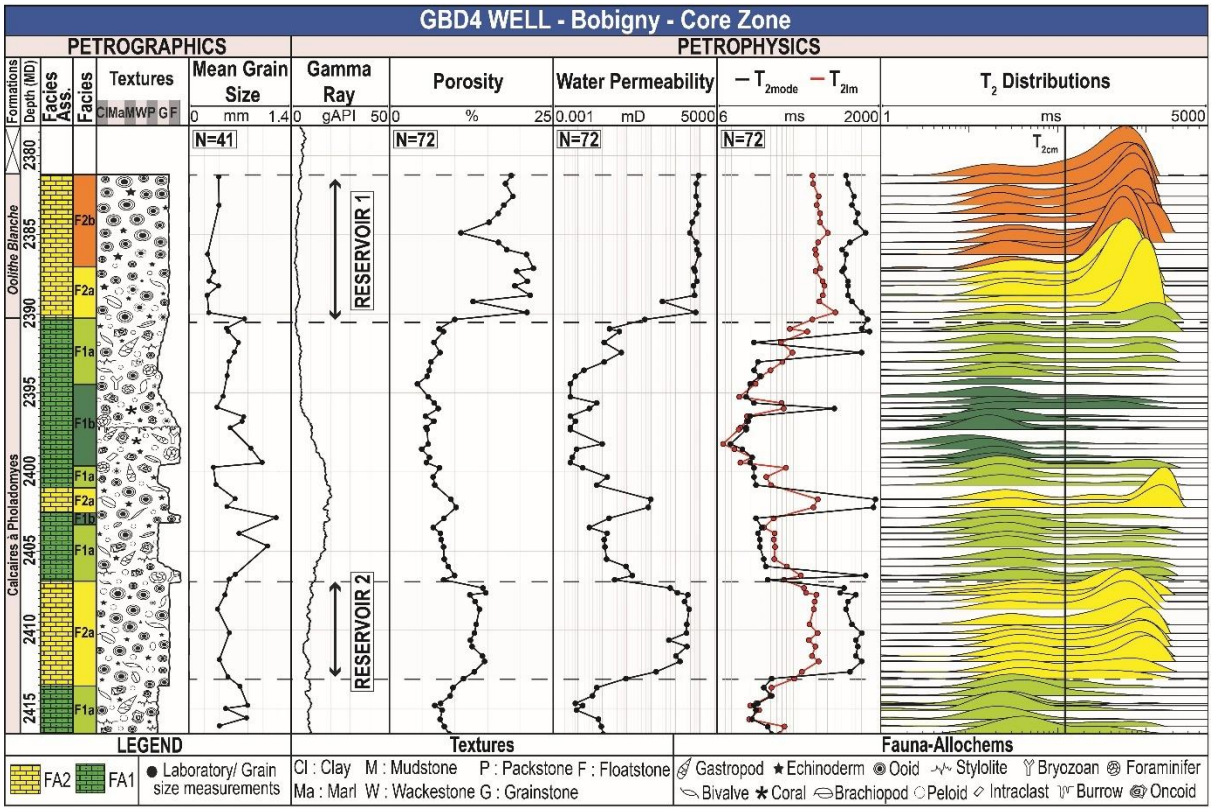

Fig. 5: Laboratory measurement results for the GBD4 core zone from 2381 to 2417 m MD (Measured Depth).

NMR T_2 distributions which were grouped depending on previously defined facies (Fig. 6) emphasize the general characteristics of the pore-size distributions of each facies. The results illustrate a strong correlation between petrophysical and petrographic observations where T_2 distributions are clearly linked to facies. The specific interpretations of NMR T_2 distributions grouped according to the proposed facies are:

(1) Facies F1a displays bimodal T_2 distributions (n=27) with a dominant mode at 30 ms corresponding to a major microporous medium, and a subsidiary mode at 1000 ms illustrating a volumetrically minor macroporosity (Fig. 6). These results are consistent with the abundant blue-to-green microporosity

observed on thin sections. Microporous networks mainly developed within muddy matrices but also in micrite forming oncoidal grains as well as in the cortex of oncoids/ooids. The addition of a secondary T_2 mode at longer relaxation times is explained by individual macropores created by some bioclastic components dissolution but also by scarce dolomite dissolution in samples n°18, 20 and 50 (Fig. 6). The NMR T_2 microporosity mode is well confirmed by low porosity values ranging from 5.8% to 10% with a mean of 7.8%, low pore throat diameter (0.1 µm), and permeability from 0.008 mD to 5.5 mD with a mean of 0.42 mD (Fig. 6).

(2) Facies F1b shows unimodal and relatively symmetrical NMR T_2 distributions (n=13) with a dominant T_2 mode at nearly 20 ms (Fig. 6) and especially for samples with the lowest permeabilities (6 in number, equal of 0.005 mD) at nearly 15 ms. These are consistent with petrographic observations showing a very poorly developed porous network. A few samples display faintly bimodal distributions with a supplementary T_2 mode above 120 ms, highlighting some macroporosity. This could be explained by the presence of scattered mouldic pores such as those observed in sample 43 within coral fragments (Fig. 6). This facies is characterized by porosity values fluctuating between 4.2% and 8.3% with an average of 6%, pore throat diameters between 0.1 µm and 0.2 µm, and permeabilities between 0.005 mD and 0.19 mD with an average calculated at 0.03 mD (Fig. 6).

(3) Facies F2a presents NMR T_2 distributions (n=21) of high amplitude for T_2 times exceeding 120 ms describing a very well-developed macroporous network (Fig. 6). A slight shoulder at low T_2 times is also noticed at nearly 35 ms (Fig. 6). Signals with the highest amplitude can be explained by dolomite dissolution processes (samples n°12, 13, 14, 15 and 17) that significantly enhance the porous media as shown by several permeability values exceeding 530 mD (being in the range of F2b values see below). Such values are consistent with petrographic observations where pores from dolomite dissolution were considerably enlarged and connected to interparticle macropores, thus facilitating fluid flow in spite of locally higher cemented areas. Major distributions of lower T_2 mode exhibit a lower volume of macropores owing to the local development of blocky cements reducing macropore volumes. The porosity values lie between 9.3% and 21.4% with an average of 14.6%, and permeability values between 0.93 mD and 740 mD with an average of 261 mD, respectively.

(4) NMR T_2 distributions of facies F2a and F2b are very similar, being bimodal with a slight shoulder at low T_2 times under 100 ms (Fig. 6). However, by focusing exclusively on F2b signatures, all of the distributions (n=11) are characterised by higher dominant T_2 mode values. This can be explained by blocky calcite developed in minor proportions thereby preserving the primary interparticle porosity which is volumetrically more dominant. Thus, this facies displays high permeability values exceeding 350 mD with a maximum of 900 mD and a mean of 694 mD, while most porosity data exceed 15% with a mean of 17.5% (Fig. 6).

The NMR T_2 distributions are relatively homogeneous for each facies and seem to be independent from the variability of the mean grain size in a same facies (Fig. 6). The mean grain size variations (from 0.3 mm to 1.2 mm) observed in a same facies association (i.e. facies F1a and F1b) do not seem to control the porosity distribution. This can be explained by the predominant mud-dominated fabric of these samples with microporosity development in micritic matrix. For facies F2a and F2b characterized by smaller mean grain sizes (from 0.24 mm to 0.62 mm), the porosity values are higher and tend to finely increase as grain sizes decrease (see Supplementary Table A).

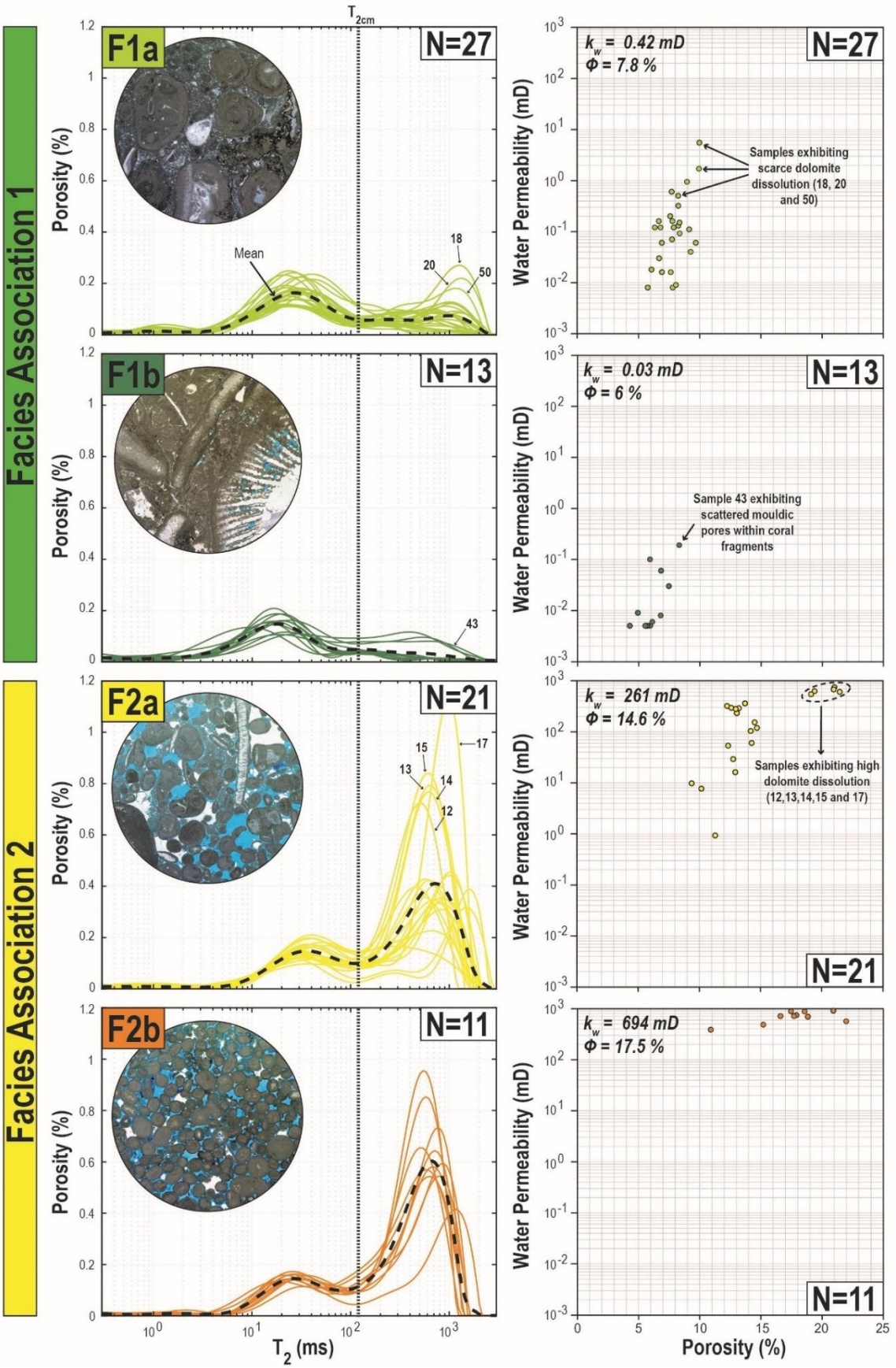

Fig. 6: NMR T_2 distribution classification results and related petrophysical properties (ϕ, k_w) according to facies definition. The mean distribution is shown by a black dashed line and average porosity and permeability values are provided for each facies.

4.1.3. T_2 distribution groups from clustering statistics

Some T_2 distributions of facies F2a (samples n°12, 13, 14, 15 and 17) are very similar to the T_2 distribution of facies F2b (Fig. 6). Similarly, some T_2 distributions of facies F1a and F1b appear very similar (Fig. 6). In order to test the sedimentary facies control on T_2 distributions, a blind classification using the k-means algorithm, i.e. without considering the previously observed facies, was performed. Interestingly, the best results are found by setting the number of clusters to k=3, combining within the same cluster (cluster 1) the distributions characterizing facies F1a and F1b (Fig. 7). It is also interesting that the T_2 distributions of F2a and F2b facies are differentiated (Fig. 7). This statistical method confirms some of the exceptions mentioned earlier, such as samples n°12, 13, 14, 15 and 17, which are closer to facies F2b than F2a (Fig. 7). The three classes defined are clearly distinguishable by their different porosity ranges when the ϕ -k_w values are plotted (Fig. 7). In this way, some distributions characterized by facies with high porosity values, such as those observed for facies F2a with some pores enlarged by dolomite dissolution processes, were assigned to the third cluster. These results highlight the fact that the variability of the four facies observed does not strictly correspond to the statistical classes in petrophysical terms (three in number) due to similar characteristics of facies F1a and F1b, and to a lesser degree between facies F2a and F2b (Fig. 7). This means that the pore networks, and subsequently the ϕ -k_w couples, are not necessary always controlled by their depositional environments but instead by the diagenetic modifications they underwent after deposition, here due to dolomite dissolution.

In a simple way, the impermeable or weakly permeable facies F1a and F1b show NMR-patterns mostly below 120 ms (i.e. a large proportion of microporosity), while the more permeable facies F2a and F2b display NMR-patterns far above 120 ms and with large intensities (i.e. a large proportion of macroporosity).

Therefore, it is mostly the interplay and organization of the micro- and macroporosity in samples that drives the permeability pattern. In this study, two different cases can be distinguished overall. In the first case, permeability is mainly governed by macropores volume (i.e. samples with a dominant connected macroporous network) regardless of the contribution from micropores to the total porosity. Such is the case for facies F2a and F2b marked by high permeability values (Fig. 7) with a strong diagenetic control (i.e. limited blocky calcite cementation and extensive dolomite dissolution processes, hence preserving or enhancing the initial porous network structure by secondary porosity development). In the second case, if the micropores are dominant (i.e. mainly in the micritic matrix), the flow in macropores is limited by contiguous microporous zones, and permeability is low, but porosity not necessarily so (i.e. due to mouldic rhombohedral macropores such as a few dolomite dissolution rhombs that do not significantly contribute to flow but which help to increase the total pore volume). Such is the case for facies F1a and F1b being characterised by low permeability values (Fig. 7) that is mainly controlled by depositional environment features (i.e. the abundant presence of carbonate mud deposits).

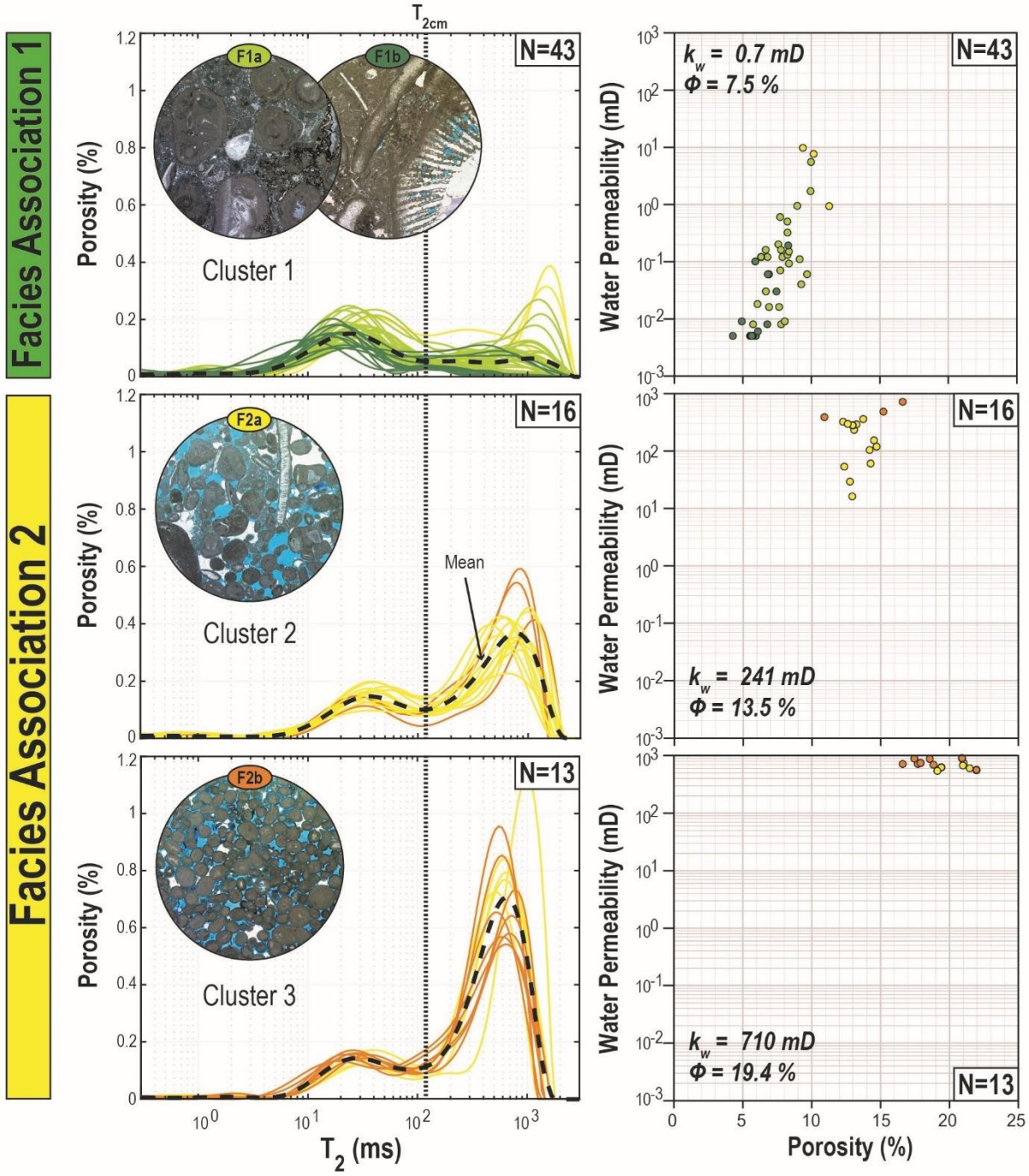

Fig. 7: Classification results of statistical analysis and related petrophysical properties (ϕ, k_w). Each NMR T_2 distribution is clustered by its similarities regardless of facies classification.

4.2. Permeability, porosity and T_2 relationships

In this section, the different relationships based on the dataset previously described and summarized in Table 2 are tested. To evaluate a given relationship, the standard deviation calculated between measured and predicted permeabilities were used. By considering power laws, a standard deviation value of 3, for instance, means that the predicted permeability k_w can statistically lie between k_w/3 and k_w*3 with a 95% confidence interval.

Name	Relationship	Parameter values	Standard deviation
k_1	$k_w = C\ \phi^n$	C = 5.81x10^9 n = 9.34	4.49
k_2	$k_w = C\ T_{2mode}^n$	C = 4x10^{-4} n = 1.83	11.71
k_3	$k_w = C\ T_{2lm}^n$	C = 2.35x10^{-8} n = 4.2	6.5
k_4	$k_w = C\ \phi^a\ T_{2lm}^b$	C = 1859 a = 6.29 b = 1.77	3.50
k_{SDR}	$k_w = C\ \phi^a\ T_{2lm}^b$	C = 4 a = 4 b = 2	4.27
k_5	$k_w = C\ \phi_m^n$	C = 3.15x10^7 n = 5.31	2.63

Table 2: Summary of the different relationships tested and the related uncertainty factors (standard deviation).

4.2.1. The permeability *versus* porosity relationship

In sandstone formations, the relationship between porosity and permeability is well constrained (Zinszner and Pellerin, 2007). In contrast, limestone formations are highly heterogenous exhibiting various and irregular pore geometries, making it difficult to derive reliable porosity-permeability correlations (Ehrenberg and Nadeau, 2005; Ehrenberg et al., 2006; Bohnsack et al., 2020). Based on cored plug measurements, permeability-porosity relationships were grouped into three classes (Lucia, 1995) (see also Fig. 8):

- Class 1: $k = (45.35\text{x}10^8)\ \phi^{8.537}$
- Class 2: $k = (2.040\text{x}10^6)\ \phi^{6.38}$
- Class 3: $k = (2.884\text{x}10^3)\ \phi^{4.275}$

where k is the permeability in millidarcy and ϕ the fractional interparticle porosity.
Each petrophysical class is related to typical pore-size distributions controlled by texture, sorting and grain size. Class 1 contains grain-dominated limestones without mud (i.e. grainstone) with large grains and the best sorting. Class 2 is characteristic of grain-dominated limestones in a mud matrix (i.e. packstone) with a decrease in grain content, size and sorting and Class 3 is defined by mud-dominated limestones (i.e. mudstone to wackestone) with a limited abundance of grains. Porosity and permeability values of GBD4 are plotted in Fig. 8. The porosity-permeability relationship valid for the present dataset is expressed as:

$$k_1 = (5.812\text{x}10^9)\ \phi^{9.34} \qquad [3]$$

The high calculated exponent of 9.34 is qualitatively in agreement with class 1 (exponent 8.537); however, the standard deviation of 4.49 indicates considerable uncertainty, characterising a weak relationship.

Porosities for facies F1a, F1b and F2a appear to be better permeability indicators than for facies F2b where permeabilities trend clearly independently of porosities. For porosities ranging from 11% to 22%, permeabilities are very homogeneously distributed and nearly constant at around 700 mD, meaning that water flows are mainly controlled by the macropore network rather than the microporosity fraction (i.e. the average macroporosity for samples F2b is nearly equal to 73%, the highest value of the dataset) (Fig. 8).

When plotted according to Lucia's classes, facies F2a and F2b belong to the first class, which is consistent with the nature of these samples (i.e. grainstone). Facies F1a (packstone to rudstone) and F1b (wackestone to floatstone) are both assigned to classes 2 and 3, which are generally consistent with previous described textures related to Lucia's classes (Fig. 8). Samples F1b with the lowest permeabilities come closer to class 3. Nevertheless, facies F1a and F1b are characterized by heterogeneous, poorly sorted fabrics, with mud-dominated matrices, which is quite consistent with both previously defined classes.

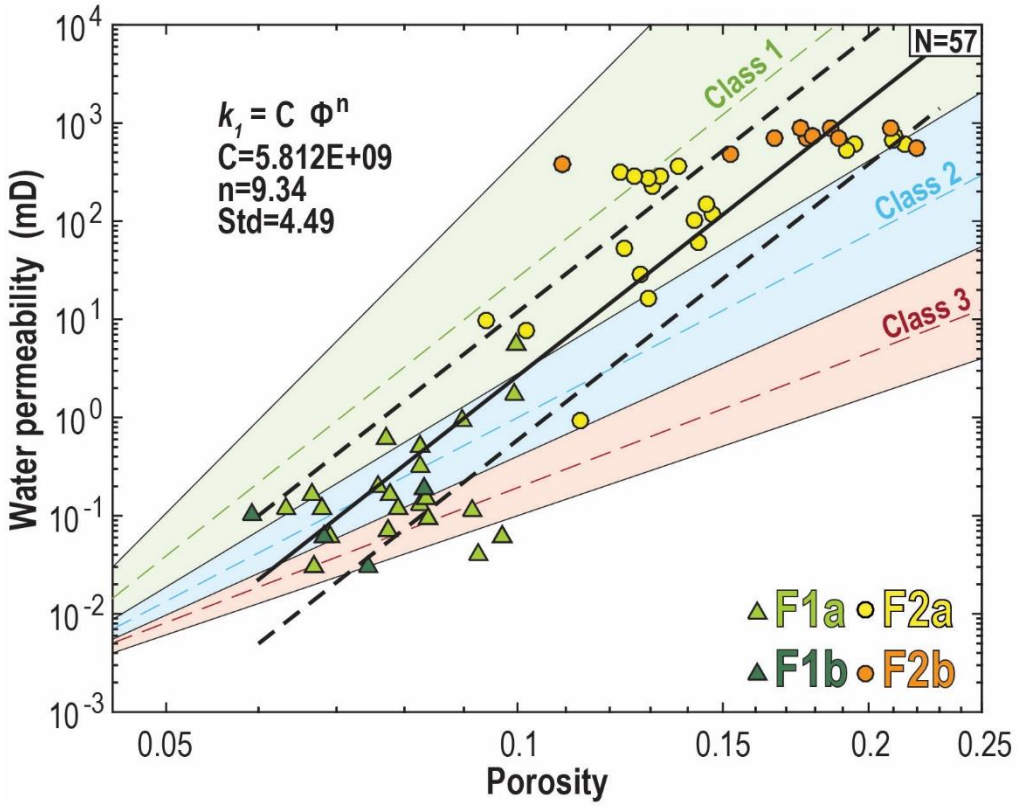

Fig. 8: Cross-plot of the porosity (ϕ) – water permeability (k_w) dataset derived from GBD4 core samples. Each point is assigned to a specific facies. The standard deviation range is illustrated by the dashed lines meaning that 95% of the predicted permeability values will lie within them. Note the logarithmic scale of both permeability and porosity axes are to be compared with predefined classes from Lucia's classification in background.

4.2.2. The permeability *versus* T_{2mode}/T_{2lm} relationship

Here, the objective is to test whether permeability can be predicted from pore size characteristics independently of porosity. For this purpose, two different approaches have been investigated: i.e. (1) using the dominant pore size (T_{2mode}) and (2) the average pore size (T_{2lm}). When plotting water permeability *versus* T_{2mode}, it is interesting to note that two main groups appear, along with a more marginal third group as shown in Fig. 9A.

A first group (Group 1) is characteristic for limestones with an average NMR-mode at 25 ms typical of the very slightly porous or microporous, mud-dominated samples F1a and F1b, which are the least permeable facies and where the amount of micropores exceeds that of macropores (Fig. 9A). A second group (Group 2), with an average dominant NMR-mode at 700 ms highlights the most permeable facies, describing a dominant macropore volume (Fig. 9A), which is consistent with petrographic observations of facies F2a and F2b. Interestingly, a third group (Group 3) displaying predominant NMR-modes mostly higher than 1000 ms are characterized by lower permeabilities than the second group (Fig. 9A). For the F1a samples, the micrite volume is significant, with well-developed micropores. However, some major rhombohedral pores formed by dolomite dissolution characterizes the bulk of the total pore volume in samples n°18, 20 and 50, resulting in dominant modes with higher relaxation times (Fig. 9A). These voluminous pores, which are individual and weakly connected to the porous network, contribute only marginally to flow (from 0.3 mD to 5.5 mD). In contrast, the higher dominant mode for samples n°19 and n°22 can be explained by a more frequent intergranular macroporosity limited by cemented areas. The microporous network is also slightly less developed leading to a decrease in permeability values (0.2 mD and 0.6 mD respectively). For the two F2a samples (n°41 and 42) in Group 3 (Fig. 9A), in which very fine and well-sorted grains alternate with coarser but heavily cemented grains, both permeabilities are much lower than in Group 2 (9.7 mD and 7.6 mD, respectively). The isolated point identified as facies F1b (sample n°29) is not easily interpretable (Fig. 9A). This sample is described by an abundant non-porous mud matrix between the grains and displays nearly equal dominant modes (i.e. 0.1% and 0.11% in amplitude). Some mouldic pores (i.e. comparable to macropores) can potentially explain the T_2 dominant mode value at nearly 400 ms, but the permeability value (of 0.03 mD) is still consistent with

other samples corresponding to this facies F1b. Summing up, these outliers reflect nearly equal amounts of micro- and macropores for these samples, so the mode may take either a low or a high value (high in this case). Thus, selecting a T_{2mode} as a single representative pore size may be a suitable option in the case of Groups 1 and 2, but it may also be not suitable if not misleading when dealing with outlying values as observed in Group 3. Therefore, a weak correlation is found along with a high standard deviation of 11.71:

$$k_2 = (4.007\text{x}10^{-4})\ \mathrm{T}_{2\mathrm{mode}}^{1.83} \quad [4]$$

Note, however, a high consistency of the first two petrophysical groups with the facies descriptions in terms of dominant pore volumes, although the samples in the third group significantly affect the robustness of the calculated relationship.

Within Fig. 9B, the data are less disparate, and the derived relationship has a lower standard deviation of 6.5, implying a slightly more robust correlation:

$$k_3 = (2.352\text{x}10^{-8})\ T_{2lm}^{4.2} \quad [5]$$

Without considering any porosity parameters, at this point, T_{2lm} seems to be a more reliable indicator when estimating permeability than T_{2mode}, based on the standard deviations of the two relationships, even though the results are not yet satisfactory.

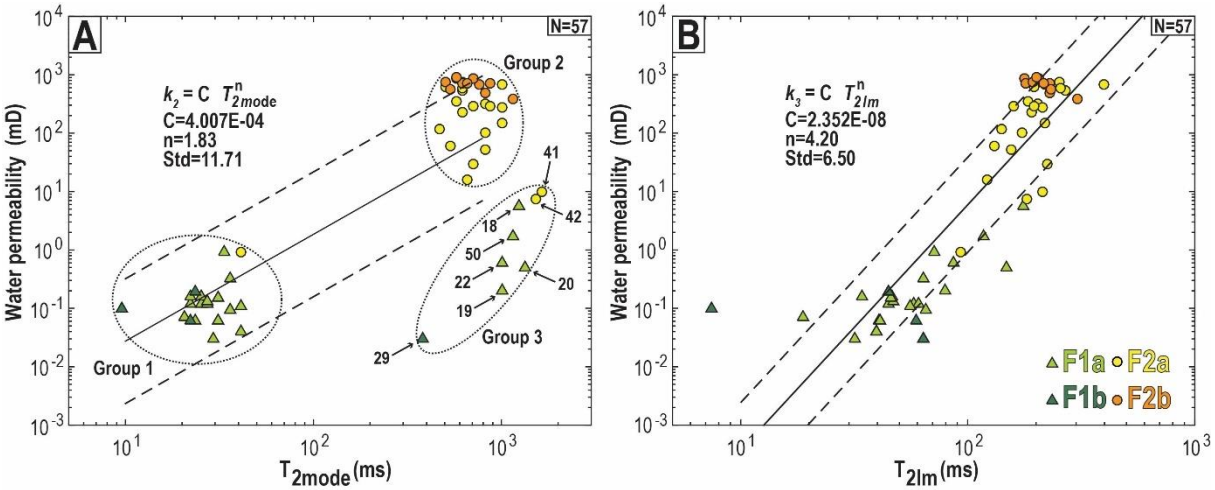

Fig. 9: A: Cross-plot of the T_{2mode} and permeability dataset derived from GBD4 core samples. B: Cross-plot of T_{2lm} and permeability. Each point relates to a specific facies and the numbers of the samples in Group 3 are annotated.

4.2.3. The permeability-porosity-T_2 relationship

Without any calibration, permeability is calculated from NMR well-log data using the Schlumberger Doll Research (SDR) equation:

$$k_{SDR} = \mathrm{C}\ \phi^{4}\ T_{2lm}^2 \quad [6]$$

However, based on laboratory data, the exponents and the constant C can be recalibrated (Fig. 10A):

$$k_4 = 1859\ \phi^{6.29}\ T_{2lm}^{1.77} \quad [7]$$

The standard deviation of 3.5 is smaller than those calculated for the three relationships previously discussed. In addition, it is noteworthy that the exponents found are similar to those proposed in the default k_{SDR} relationship (exponent a = 6.29, close to 4, and exponent b = 1.77, close to 2) (Fig. 10B). Note also that the “a” exponent is slightly higher, reflecting greater sensitivity to porosity. These results demonstrate that the new k_4 equation predicts permeability more accurately than the initial default k_{SDR} equation, which yielded an uncertainty factor of 4.27 (Fig. 10B). The k_4 equation improves the previous simple porosity to permeability relationship, although only moderately. This new equation can therefore be used for the middle Jurassic limestones, at least for the four facies identified whenever NMR logs are available.

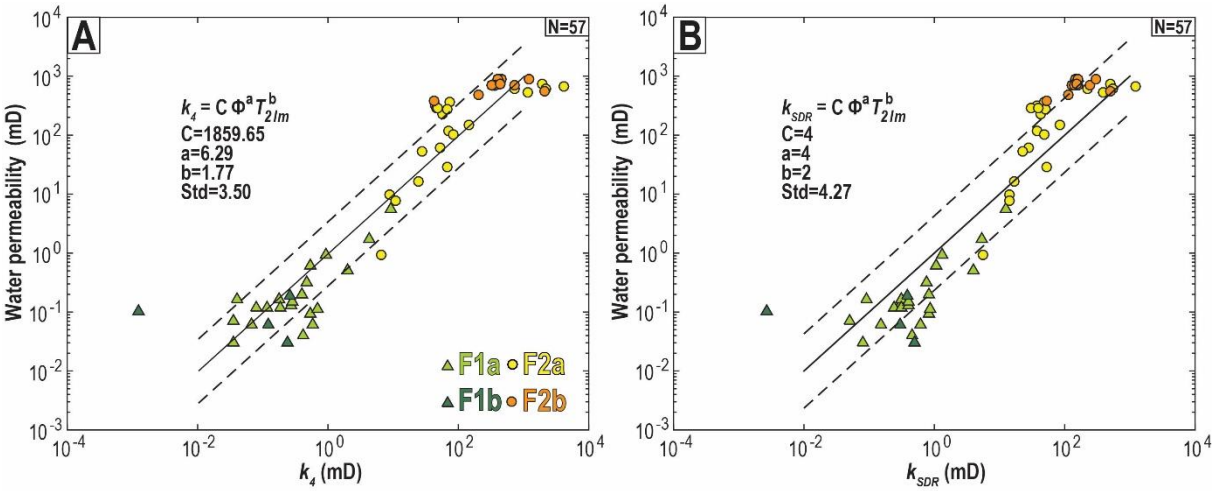

Fig. 10: A: Optimum permeability prediction using exponents a and b fitted to data. B: Permeability prediction using the SDR equation.

4.2.4. The permeability *versus* macroporosity relationship

To further improve permeability predictions, several authors proposed various other relationships that may be valid for carbonate systems (Aghda et al., 2018; Ge et al., 2017; Mason et al., 2019). For instance, new parameters could be added by subdividing the T_2 distribution into more intervals in addition to micro- and macropores, and also to include for example mesopores (Ge et al., 2017). However, a much simpler approach by calculating the amount of macroporosity from T_2 distributions is suggested here. The dividing line separating microporosity from macroporosity was set at 120 ms (Fig. 2), which is a slightly lower value than that determined in previous work (Vincent et al., 2011).

With a simple power law linking k_w *versus* macroporosity ϕ_m (Fig. 11) an uncertainty factor of 2.63 was obtained, the lowest of all the investigated relationships. It is important to mention that six points with a macroporosity of less than 0.02 were omitted from this fitting exercise. Such samples with the lowest macroporosity values do not contribute to flow, i.e. they typically have low permeabilities with an average of 0.08 mD. The best relationship corresponds to:

$$k_5 = (3.15\text{x}10^7)\,\phi_m^{5.31} \quad [8]$$

There is a good correlation between permeability and macroporosity within the used dataset (Fig. 11). The standard deviation of 2.63 is the lowest of all the studied relationships (Table 2).

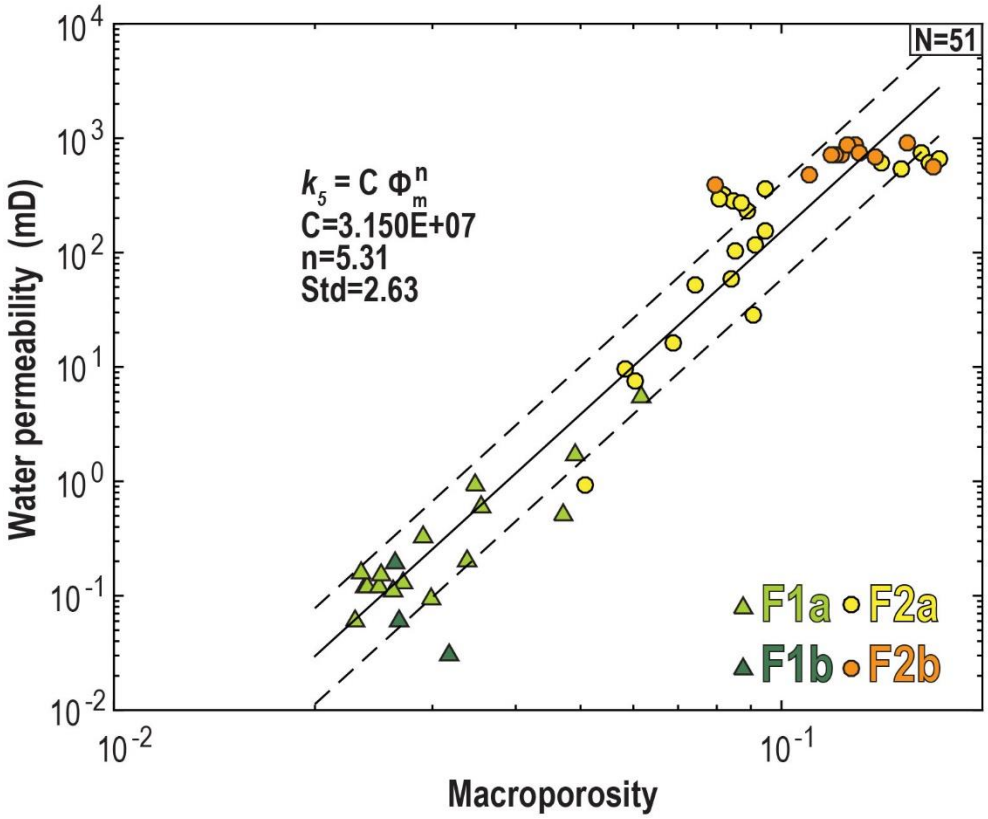

Fig. 11: Permeability prediction using macroporosity derived from a cut-off at 120 ms.

5. –Conclusions

A laboratory study was presented comprising 72 measurements of porosity, permeability and NMR T_2 distributions for a world-class carbonate geothermal reservoir i.e. the *Oolithe Blanche* Formation in the Paris Basin (France). Petrographic investigations of core samples allowed to define four facies, grouped into two facies associations, two of them being mud-supported limestones (FA1) indicating a distal environment (upper offshore) and presenting poor reservoir properties and two others being macroporous grainstones (FA2) deposited in a more proximal shoreface/shoal environment displaying high reservoir properties. Facies F2b displays abundant ooids and is very weakly cemented with blocky calcite content or syntaxial calcite cement, giving rise to this facies its good reservoir quality. This facies is characterized by almost constant permeabilities of around 700 mD, porosities ranging from 11% to 22% and pore throat diameter of 50 µm. Facies F2a is more cemented, but its reservoir quality remains as relatively high. In particular for this facies, five samples are similar to facies F2b in terms of petrophysical responses. This is due to dolomite dissolution processes, carefully deduced by observation of pore boundaries, locally forming rhombohedral pore shapes (rhomb terminations at some points or flat surface). This dolomite dissolution significantly enhancing porosity and permeability values, thereby demonstrating that the structure of the pore network can be greatly affected by diagenetic changes.

This study can be used in four ways; (i) in the case NMR well-logs are not available and one has to rely on porosity alone to predict permeability. Accordingly a permeability vs. porosity relationship can be used ($k_1 = (5.812\text{x}10^9)\ \phi^{9.34}$), albeit with considerable uncertainty (standard deviation of 4.49), to predict permeability from total porosity (e.g. from neutron porosity logs) at least for the two facies associations. (ii) Another valid option would be to assign a single permeability value for facies F2b if this facies is identified in other wells for which no experimental measurements have been made. This could prove a useful option for geothermal reservoir modelling if no supplementary well-logs are recorded to assign a single given value, or a minimum and/or maximum and a low standard deviation for a given facies when building the permeability model.

(iii) In the case NMR well-logs are available, an optimum relationship ($k_4 = 1859\ \phi^{6.29}\ T_{2lm}^{1.77}$) was found when combining porosity and a mean pore size described by T_{2lm}. This relationship should be used instead of the standard SDR relationship provided in well-log data analysis because the standard deviation decreases from 4.27 to 3.5. (iv) However, the best permeability prediction is achieved with a

single parameter, macroporosity ϕ_m, calculated from the T_2 distributions and using a cut-off value at 120 ms ($k_5 = (3.15\text{x}10^7)\ \phi_m^{5.31}$). Indeed, this relationship has the lowest statistical uncertainty (2.63). Macroporosity determines flow in these complex porous structures, whereas microporosity influences the total porosity in such a way that the permeability-porosity correlation is greatly modified, yielding very unreliable predictions.

This work thus provides sound guidance when using NMR logs (1) to characterize reservoir quality and well performance in geothermal studies and (2) to optimize locations for future geothermal projects in the suburban areas of Paris.

Acknowledgements

This work is supported by the UPGEO “UPscaling and heat simulations for improving the efficiency of deep GEOthermal energy” programme funded by the Agence Nationale de la Recherche [ANR-19-CE05-0032-01]. This work is also supported by GEOFLUID [2019-0164] and by the Paris Region PhD programme funded by the Ile-de-France Regional Council [2019-0309]. We thank Phillipe Blanc (from Lithologie Bourgogne) and Valérie Godard for thin-section preparation and Jean Guelard (from IFPen) for lab measurements. University Paris-Saclay benefits from the Schlumberger Software Donation Programme. We are grateful to Schlumberger for the academic licence for Petrel© software and for very valuable support in its utilization. We also thank two anonymous reviewers who provided insightful and helpful comments that improved the final manuscript.

Data availability

Datasets are available as Supplementary Tables. Supplementary Table A, an Excel Sheet, summarizes the mean grain sizes values and related standard deviation of 41 samples (with thin section). Supplementary Table B, an Excel Sheet, summarizes the pore throat distribution obtained by mercury injection capillary pressure (MICP) for 4 samples. Supplementary Table C summarizes, by sample, facies association, facies, location on core (depth), porosity, macroporosity, permeability, T_{2mode}, T_{2LM}, formation factor and thin section. Supplementary Table D, an Excel Sheet, summarizes the T_2 distribution of the 72 samples.

Appendices

Supplementary Table A: Summary of the mean grain sizes values and related standard deviation of 41 samples with thin section (Excel Sheet).

Supplementary Table B: Summary of the pore throat distributions obtained by mercury injection capillary pressure (MICP) for 4 samples (Excel Sheet)

Supplementary Table C: Summary of the various petrophysical measurements (permeability, formation factor) and deduced variables (NMR porosity, macroporosity, T_{2mode}, T_{2lm}) for each GBD4 (Bobigny 4 well) core sample. Each sample is associated with the corresponding facies and facies association (Facies Ass.). The samples used for making thin sections are also mentioned. Na: Not available.

Sample	Facies Ass.	Facies	Measured depth (m)	Porosity (%)	Macroporosity (%)	Permeability (mD)	T_{2mode} (ms)	T_{2lm} (ms)	Formation factor	Thin section
1	FA2	F2b	2381.3	18.6	12.9	870	580	177	25.8	x
2	FA2	F2b	2381.8	17.7	12.3	710	622	180	Na	
3	FA2	F2b	2382.6	18.8	13.7	690	766	219	30.5	
4	FA2	F2b	2383.1	17.5	12.5	880	714	205	Na	x
5	FA2	F2b	2383.6	16.6	12.0	710	880	230	33.8	
6	FA2	F2b	2384.2	15.2	10.9	480	821	229	Na	
7	FA2	F2b	2384.9	10.9	7.94	384	1162	303	25.4	
8	FA2	F2b	2385.5	16.6	11.8	710	667	215	Na	
9	FA2	F2b	2385.9	17.9	13.0	740	505	194	14.5	
10	FA2	F2b	2386.2	20.9	15.4	900	580	200	Na	x
11	FA2	F2b	2387.1	21.9	16.9	560	541	231	23.7	
12	FA2	F2a	2387.3	19.4	14.0	620	505	196	Na	x
13	FA2	F2a	2387.9	21	16.2	740	622	252	26.3	x
14	FA2	F2a	2388.2	19.1	15.1	540	622	269	Na	x
15	FA2	F2a	2388.8	21.5	16.6	600	622	255	53.1	x
16	FA2	F2a	2389.2	12.8	9.07	29	715	224	Na	
17	FA2	F2a	2389.9	20.9	17.2	670	1011	398	89.5	x
18	FA1	F1a	2390.3	9.9	6.15	5.5	1246	175	Na	x
19	FA1	F1a	2390.9	7.6	3.37	0.2	1011	79	158.7	x
20	FA1	F1a	2391.1	8.2	4.69	0.5	1335	147	Na	x
21	FA1	F1a	2391.8	6.8	2.37	0.12	22	58	140.6	x
22	FA1	F1a	2392.4	7.7	3.55	0.6	1011	87	Na	x
23	FA1	F1a	2393	6.3	2.39	0.12	25	61	212.5	x
24	FA1	F1a	2393.6	6	1.77	0.02	22	40	Na	
25	FA1	F1a	2393.9	5.7	1.04	0.008	27	28	Na	x
26	FA1	F1b	2394.4	4.2	0.56	0.005	19	23	Na	
27	FA1	F1b	2395.2	5.9	0.60	0.005	17	13	Na	x
28	FA1	F1b	2395.6	6.8	2.67	0.06	22	56	Na	
29	FA1	F1b	2395.9	7.5	3.17	0.03	383	64	Na	x
30	FA1	F1b	2396.5	5.5	0.58	0.005	19	17	Na	x
31	FA1	F1b	2396.8	6.8	0.63	0.008	18	17	Na	x
32	FA1	F1b	2397.2	5.6	0.51	0.005	17	14	Na	x

33	FA1	F1b	2397.3	5.7	0.40	0.005	17	13	Na		
34	FA1	F1b	2398.2	5.9	0.46	0.1	10	7	Na		
35	FA1	F1b	2398.5	4.9	0.32	0.009	15	11	Na		x
36	FA1	F1b	2399	6.1	0.77	0.006	21	21	Na		
37	FA1	F1b	2399.4	5.6	0.59	0.005	19	14	159.7	x	
38	FA1	F1a	2399.7	7.6	2.98	0.016	22	69	Na		x
39	FA1	F1a	2400.3	6.8	1.28	0.16	22	34	140.1		
40	FA1	F1a	2400.8	6.9	1.89	0.06	24	40	Na		x
41	FA2	F2a	2401.7	9.4	5.84	9.7	1645	213	Na		x
42	FA2	F2a	2402.2	10.2	6.05	7.6	1534	182	116.9		x
43	FA1	F1b	2402.9	8.3	2.63	0.19	24	44	Na		x
44	FA1	F1a	2403.5	6.7	1.27	0.03	29	32	Na		
45	FA1	F1a	2403.9	7.8	2.34	0.16	25	46	Na		x
46	FA1	F1a	2404.3	7.9	2.50	0.12	27	45	Na		
47	FA1	F1a	2404.7	8.3	2.71	0.13	27	47	Na		x
48	FA1	F1a	2405.5	8.4	2.51	0.15	31	46	92.3		
49	FA1	F1a	2405.9	8.9	3.48	0.94	34	71	Na		
50	FA1	F1a	2406.5	9.9	4.92	1.7	1162	117	110		x
51	FA1	F1a	2406.8	8.2	2.90	0.32	36	64	Na		x
52	FA2	F2a	2407.3	14.3	8.42	60	542	131	46.1		
53	FA2	F2a	2407.6	14.7	9.14	118	471	141	Na		
54	FA2	F2a	2407.8	12.3	8.19	318	821	203	34.47		x
55	FA2	F2a	2408.2	13	8.86	231	622	190	Na		
56	FA2	F2a	2408.7	13.7	9.42	357	580	185	35.52		x
57	FA2	F2a	2409.6	13.2	8.45	288	715	159	Na		
58	FA2	F2a	2410.2	12.9	8.68	277	1012	212	41.85		x
59	FA2	F2a	2410.6	12.4	7.44	53	821	155	Na		
60	FA2	F2a	2411	12.6	8.05	293	880	196	44.11		
61	FA2	F2a	2411.6	14.2	8.53	103	821	173	Na		
62	FA2	F2a	2411.9	14.5	9.45	152	1012	220	51.09		x
63	FA2	F2a	2412.6	12.9	6.88	16	667	121	Na		
64	FA2	F2a	2413	11.3	5.09	0.9	41	93	Na		x
65	FA1	F1a	2413.6	9.7	2.29	0.06	31	41	Na		x
66	FA1	F1a	2414.1	9.3	1.61	0.04	41	39	Na		
67	FA1	F1a	2414.6	7.8	0.72	0.008	26	24	Na		
68	FA1	F1a	2414.8	6.9	0.63	0.016	22	19	Na		x
69	FA1	F1a	2415	8	0.98	0.009	24	27	Na		x
70	FA1	F1a	2415.6	7.7	0.45	0.07	21	19	Na		x
71	FA1	F1a	2416.1	8.4	2.99	0.09	36	65	Na		x
72	FA1	F1a	2416.6	9.1	2.61	0.11	41	56	Na		

Supplementary Table D: Distribution of T_2 time for each sample (Excel Sheet).

References

Aghda, S.M.F., Taslimi, M., Fahimifar, A., 2018. Adjusting porosity and permeability estimation by nuclear magnetic resonance: a case study from a carbonate reservoir of south of Iran. J Petrol Explor Prod Technol 8, 1113–1127. https://doi.org/10.1007/s13202-018-0474-z

Allo, F., Coulon, J.-P., Formento, J.-L., Reboul, R., Capar, L., Darnet, M., Issautier, B., Marc, S., Stopin, A., 2021. Characterization of a carbonate geothermal reservoir using rock-physics-guided deep neural networks. The Leading Edge 40, 751–758. https://doi.org/10.1190/tle40100751.1

Antics, M., Papachristou, M., Ungemach, P., 2005. Sustainable heat mining. A reservoir engineering approach. Proceedings, thirtieth Workshop on Geothermal Reservoir Engineering. Stanford University. 14.

Appel, M., Radcliffe, N.J., Aadireddy, P., Bonnie, R.J.M., Akkurt, R., 2003. Nuclear Magnetic Resonance While Drilling in the Southern North Sea. SPE Reservoir Evaluation & Engineering 6, 351–360. https://doi.org/10.2118/86915-PA

Babadagli, T., Al-Salmi, S., 2004. A Review of Permeability-Prediction Methods for Carbonate Reservoirs Using Well-Log Data. SPE Reservoir Evaluation & Engineering 7, 75–88. https://doi.org/10.2118/87824-PA

Banavar, J.R., Schwartz, L.M., 1987. Magnetic resonance as a probe of permeability in porous media. Phys. Rev. Lett. 58, 1411–1414. https://doi.org/10.1103/PhysRevLett.58.1411

Bohnsack, D., Potten, M., Pfrang, D., Wolpert, P., Zosseder, K., 2020. Porosity–permeability relationship derived from Upper Jurassic carbonate rock cores to assess the regional hydraulic matrix properties of the Malm reservoir in the South German Molasse Basin. Geotherm Energy 8, 12. https://doi.org/10.1186/s40517-020-00166-9

Bonté, D., Guillou-Frottier, L., Garibaldi, C., Bourgine, B., Lopez, S., Bouchot, V., Lucazeau, F., 2010. Subsurface temperature maps in French sedimentary basins: new data compilation and interpolation. Bulletin de la Société Géologique de France 181, 377–390. https://doi.org/10.2113/gssgfbull.181.4.377

Bonté, D., van Wees, J.D., Guillou-Frottier, L., Bouchot, V., Serrano, O., 2013. Deep temperatures in the Paris Basin using tectonic-heat flow modelling. Proceedings of the European Geothermal Congress HS1-19, Pisa, Italy, p.10 pp. 11.

Brigaud, B., Vincent, B., Durlet, C., Deconinck, J.-F., Jobard, E., Pickard, N., Yven, B., Landrein, P., 2014. Characterization and origin of permeability–porosity heterogeneity in shallow-marine carbonates: From core scale to 3D reservoir dimension (Middle Jurassic, Paris Basin, France). Marine and Petroleum Geology 57, 631–651. https://doi.org/10.1016/j.marpetgeo.2014.07.004

Burchette, T.P., Wright, V.P., 1992. Carbonate ramp depositional systems. Sedimentary Geology 79, 3–57. https://doi.org/10.1016/0037-0738(92)90003-A

Chauveteau, G., Nabzar, L., Attar, Y.E., Jacquin, C., 1996. Pore Structure and Hydrodynamics in Sandstones. SCA paper 9607 presented at the 1996 International Symposium of the Society of Core Analysts, Montpellier, France, Sept. 8-10. 12.

Choquette, P.W., Pray, L.C., 1970. Geologic Nomenclature and Classification of Porosity in Sedimentary Carbonates. 207-250. Bulletin 54. https://doi.org/10.1306/5D25C98B-16C1-11D7-8645000102C1865D

Contini, D., Mangold, C., Enay, R., 1980. Evolution palégéographique de la France au Jurassique Moyen. In : Enay, R., Mangold, C. (Eds.), Synthèse paléogéographique du Jurassique français. pp. 66-70.

Duan, W., Zhiqian, G., Tailiang, F., Miaomiao, M., Yue, C., Yangbing, L., Chenjia, Z., 2018. New Insight into the Characteristics of Tight Carbonate based on Nuclear Magnetic Resonance. Energy Fuels 32, 2962–2972. https://doi.org/10.1021/acs.energyfuels.7b03460

Dunham, R.J., 1962. Classification of Carbonate rocks according to depositional texture. In: Ham, W.E. (Ed.), Classification of Carbonate Rocks: AAPG Mem., 1, pp. 108-121 14.

Dunn, K.-J., Bergman, D.J., Latorraca, G.A., 2002. Nuclear magnetic resonance: Petrophysical and logging applications (1st ed.). Seismic exploration : v.32. Pergamon.

Ehrenberg, S.N., Eberli, G.P., Baechle, G., 2006. Porosity-permeability relationships in Miocene carbonate platforms and slopes seaward of the Great Barrier Reef, Australia (ODP Leg 194, Marion Plateau). Sedimentology 53, 1289–1318. https://doi.org/10.1111/j.1365-3091.2006.00817.x

Ehrenberg, S.N., Nadeau, P.H., 2005. Sandstone vs. carbonate petroleum reservoirs: A global perspective on porosity-depth and porosity-permeability relationships. Bulletin 89, 435–445. https://doi.org/10.1306/11230404071

Embry, A., Klovan, J.E., 1971. A Late Devonian reef tract on northeastern Banks Island, Northwest Territories. Bull. Can. Pet. Geol., 19: 730-781 52.

Fleury, M., Deflandre, F., Godefroy, S., 2001. Validity of permeability prediction from NMR measurements. Comptes Rendus de l'Académie des Sciences - Series IIC - Chemistry 4, 869–872. https://doi.org/10.1016/S1387-1609(01)01343-3

Ge, X., Fan, Y., Liu, J., Zhang, L., Han, Y., Xing, D., 2017. An improved method for permeability estimation of the bioclastic limestone reservoir based on NMR data. Journal of Magnetic Resonance 283, 96–109. https://doi.org/10.1016/j.jmr.2017.09.004

Giot, D., Rojas, J., 1981. Caractéristiques sédimentologiques et diagraphiques du dogger dans le forage géothermique d'Aulnay-sous-Bois (Seine-Saint-Denis). Rapport BRGM 82-SGN-736-GTH.

Godefroy, S., Korb, J.-P., Fleury, M., Bryant, R.G., 2001. Surface nuclear magnetic relaxation and dynamics of water and oil in macroporous media. Phys. Rev. E 64, 021605. https://doi.org/10.1103/PhysRevE.64.021605

Guillocheau, F., Robin, C., Allemand, P., Bourquin, S., Brault, N., Dromart, G., Friedenberg, R., Garcia, J.-P., Gaulier, J.-M., Gaumet, F., Grosdoy, B., Hanot, F., Le Strat, P., Mettraux, M., Nalpas, T., Prijac, C., Rigoltet, C., Serrano, O., Grandjean, G., 2000. Meso-Cenozoic geodynamic evolution of the Paris Basin: 3D stratigraphic constraints. Geodynamica. Acta, 13, 189-246. Geodinamica Acta 13, 189–245. https://doi.org/10.1080/09853111.2000.11105372

Hamm, V., 2015. Gestion du Dogger et corrélations entre niveaux producteurs. Rapport BRGM RP-65472-FR.

Housse, B., Maget, P., 1976. Le potentiel géothermique du Bassin Parisien. Etude BRGM-SNEAP, n° 74-7-0990.

Kenyon, W.E., 1997. Petrophysical principles of applications of NMR logging. 21-43. The log Analyst.

Kenyon, W.E., Day, P.I., Straley, C., Willemsen, J.F., 1988. A Three-Part Study of NMR Longitudinal Relaxation Properties of Water-Saturated Sandstones. SPE Formation Evaluation 3, 622–636. https://doi.org/10.2118/15643-PA

Lønøy, A., 2006. Making sense of carbonate pore systems. Bulletin 90, 1381–1405. https://doi.org/10.1306/03130605104

Lopez, S., Hamm, V., Le Brun, M., Schaper, L., Boissier, F., Cotiche, C., Giuglaris, E., 2010. 40 years of Dogger aquifer management in Ile-de-France, Paris Basin, France. Geothermics 39, 339–356. https://doi.org/10.1016/j.geothermics.2010.09.005

Lucia, F.J., 2007. Petrophysical Rock Properties. In carbonate Reservoir Characterization (pp. 1-27). Springer Berlin Heidelberg.

Lucia, F.J., 1995. Rock-Fabric/Petrophysical Classification of Carbonate Pore Space for Reservoir Characterization. Bulletin 79. https://doi.org/10.1306/7834D4A4-1721-11D7-8645000102C1865D

Lund, J.W., Toth, A.N., 2021. Direct utilization of geothermal energy 2020 worldwide review. Geothermics 90, 101915. https://doi.org/10.1016/j.geothermics.2020.101915

Macqueen, J., 1967. Some methods for classification and analysis of multivariate observations. In: Proceedings of the fifth Berkeley symposium on mathematical statistics and probability. Volume 1, pages 281-297. Oakland, CA, USA. 17.

Mason, H.E., Smith, M.M., Carroll, S.A., 2019. Calibration of NMR porosity to estimate permeability in carbonate reservoirs. International Journal of Greenhouse Gas Control 87, 19–26. https://doi.org/10.1016/j.ijggc.2019.05.008

Mégnien, C., Mégnien, F., 1980. Synthèse géologique du bassin de Paris, Volume I : Stratigraphie et paléogéographie. In: Mémoire du Bureau de Recherches Géologiques et Minières, n°101, 466 pp.

Minh, C.C., Petricola, M., Dennis, B., 1997. The carbonate challenge. Middle East Well Eval. Rev. 20, 36-55.

Moss, A.K., 2000. The ART NMR Carbonate rock catalogue: a library of NMR response characteristics in carbonate rocks. DiaLog 8 (3) (online).

Müller-Huber, E., Börner, F., Börner, J.H., Kulke, D., 2018. Combined interpretation of NMR, MICP, and SIP measurements on mud-dominated and grain-dominated carbonate rocks. Journal of Applied Geophysics 159, 228–240. https://doi.org/10.1016/j.jappgeo.2018.08.011

Müller-Huber, E., Schön, J., Börner, F., 2016. Pore space characterization in carbonate rocks — Approach to combine nuclear magnetic resonance and elastic wave velocity measurements. Journal of Applied Geophysics 127, 68–81. https://doi.org/10.1016/j.jappgeo.2016.02.011

Nurmi & Standen, 1997. Carbonates: the inside story. Middle East Well Evaluation Review, 18 28–41.

Purser, B.H., 1985. Dedolomite Porosity and Reservoir Properties of Miffle Jurassic Carbonates in the Paris Basin, France, in: Roehl, P.O,. Choquette, P.W. (Eds.), Carbonate Petroleum Reservoirsn Casebooks in Earth Sciences. New York, NY, pp. 341-355. 14.

Robelin, C., Giot, D., 1987. Différenciation des ciments carbonatés par cathodoluminescence. Cas des réservoirs géothermiques du Dogger d'Aulnay-sous-Bois (Seine-Saint-Denis, France). Bulletin de la Société Géologique de France III, 1023-1032.

Rojas, J., Giot, D., Nindre, Y.M., Criaud, A., Fouillac, C., Brach, M., Menjoz, A., Martin, J.C., Lambert, M., Chiles, J.P., Fouillac, A.M., Pauwels, H., 1989. Caractérisation et modélisation du réservoir géothermique du Dogger: Bassin Parisien, France. Rapport Final BRGM EUR 12639 FR. Institut mixte de recherches géothermiques. 262.

Rojas, J., Menjoz, A., Martin, J.C., Criaud, A., Fouillac, C., 1987. Development and exploitation of low enthalpy geothermal system: example of the Dogger in the Paris Basin, France. Proc. 12th Workshop on Geothermal Reservoir Engineering. Standford, 1/1987, 203-212.

Sarker, I.H., 2021. Machine Learning: Algorithms, Real-World Applications and Research Directions. SN COMPUT. SCI. 2, 160. https://doi.org/10.1007/s42979-021-00592-x

Soete, J., Claes, S., Claes, H., Erthal, M.M., Hamaekers, H., De Boever, E., Foubert, A., Klitzsch, N., Swennen, R., 2021. Unravelling the pore network and its behaviour: An integrated NMR, MICP, XCT and petrographical study of continental spring carbonates from the Ballık area, SW Turkey. Depositional Rec dep2.135. https://doi.org/10.1002/dep2.135

Thomas, H., Brigaud, B., Blaise, T., Zordan, E., Zeyen, H., Catinat, M., Andrieu, S., Mouche, E., Fleury, M., 2023. Upscaling of Geological Properties in a World-Class Carbonate Geothermal System in France: From Core Scale to 3d Regional Reservoir Dimensions. SSRN Journal. https://doi.org/10.2139/ssrn.4097492

Tian, F., Wang, W., Liu, N., Jiang, J., Niu, C., Zhang, Y., Li, Y., 2018. Rock-Type Definition and Pore Characterization of Tight Carbonate Rocks Based on Thin Sections and MICP and NMR Experiments. Appl Magn Reson 49, 631–652. https://doi.org/10.1007/s00723-018-0993-2

Ungemach, P., Antics, M., Davaux, M., 2019. Subhorizontal well architecture enhances heat production: the Cachan limestone. European Geothermal Congress, Den Haag, The Netherlands. 14.

Vincent, B., Brigaud, B., Thomas, H., Gaumet, F., 2021. Giant subaqueous carbonate dunes: a revised interpretation of large-scale oo-bioclastic clinoforms in the middle Jurassic of the Paris Basin and its implications. Facies 67, 12. https://doi.org/10.1007/s10347-021-00621-4

Vincent, B., Fleury, M., Santerre, Y., Brigaud, B., 2011. NMR relaxation of neritic carbonates: An integrated petrophysical and petrographical approach. Journal of Applied Geophysics 74, 38–58. https://doi.org/10.1016/j.jappgeo.2011.03.002

Wadood, B., Khan, S., Liu, Y., Li, H., Rahman, A., 2021. Investigating the impact of diagenesis on reservoir quality of the Jurassic shallow shelfal carbonate deposits: Kala Chitta Range, North Pakistan. Geological Journal 56, 1167–1186. https://doi.org/10.1002/gj.3968

Westphal, H., Surholt, I., Kiesl, C., Thern, H.F., Kruspe, T., 2005. NMR Measurements in Carbonate Rocks: Problems and an Approach to a Solution. Pure appl. geophys. 162, 549–570. https://doi.org/10.1007/s00024-004-2621-3

Wielemaker, E., Cavalleri, C., Dahlhaus, L., Reynaldos, A., Sosio, G., Ungemach, P., Antics, M., Davaux, M., 2020. Delineating the geothermal structure and flow properties in a sub-horizontal well with the use of wireline and LWD data in a multiphysics approach., in: SPWLA 61st Annual Online Symposium Transactions. Presented at the 2020 SPWLA 61st Annual Online Symposium, Society of Petrophysicists and Well Log Analysts. https://doi.org/10.30632/SPWLA-5065

Zinszner, B., Pellerin, F.M., 2007. A Geoscientist's Guide to Petrophysics, Technip editions. IFP Publications. 384 pp.